International Journal of Solids and Structures 112 (2017) 106–121

Contents lists available at ScienceDirect

International Journal of Solids and Structures

journal homepage: www.elsevier.com/locate/ijsolstr

Exterior statistics based boundary conditions for establishing statistically equivalent representative volume elements of statistically nonhomogeneous elastic microstructures

Dhirendra V. Kubair, Somnath Ghosh*

Departments of Civil, Mechanical and Materials Science & Engineering, Johns Hopkins University, 3400 N. Charles Street, Baltimore, MD 21218, United States

ARTICLE INFO

Article history:
Received 22 November 2016
Revised 7 February 2017
Available online 16 February 2017

Keywords:
Heterogeneous microstructure
Statistically equivalent representative volume elements (SERVE)
Exterior statistics-based boundary conditions
Two-point correlation functions
Eshelby's solution
Clusters
Matrix-rich regions

ABSTRACT

The exterior statistics-based boundary conditions or ESBCs have been developed as optimally effective boundary conditions that can be applied to statistically equivalent representative volume elements or SERVEs of heterogeneous microstructures for predicting homogenized response functions in Ghosh and Kubair (2016). However the initial development was for nonuniform, but statistically homogeneous microstructures with no localized features like clustering. In this case, the radial distribution function $S_2(r)$ is adequate for the statistically informed Green's functions needed for the development of ESBCs. However, when the microstructure includes statistical inhomogeneities in the form of fiber clusters or matrix-rich regions, the distance-based radial distribution function becomes ineffective. This paper overcomes this shortcoming by introducing the joint, distance (radial) and orientation-based two-point correlation functions $S_2(r, \theta)$ in the statistically informed Green's functions needed for the ESBCs. The efficacy of the ESBCs is illustrated through validation simulations that compare its results with those generated by affine transformation based displacement and periodicity boundary conditions. Additionally, comparisons are made with the statistical volume elements or SVE methods. It is concluded that the simulations with ESBCs prescribed on the SERVEs have a definite advantage over other methods in defining optimal sized SERVEs without any iteration.

1. Introduction

The behavior of heterogeneous materials including composites depends on the microstructural composition, such as the morphology of constituent and reinforcing phases as well as their material properties. The overall response and property evaluation of these materials for use in macroscopic structural analysis is often conducted by hierarchical multi-scale modeling. In this process, direct numerical simulations (DNS) at the micro- or meso-scales of the material is followed by homogenization to generate effective constitutive models and parameters for higher length-scale analysis. The DNS explicitly accounts for shapes, sizes and locations of heterogeneities in the microstructure. Homogenization methods often admit the existence of microstructural representative volume elements or RVEs and subsequently apply averaging principles like the Hill–Mandel condition (Hill, 1967) with assumptions of scale-separation and energy equivalence of the RVE microstructural analyses and homogenized medium under equivalent loading conditions. Homogenization using computational micromechanical analysis for DNS of complex microstructures e.g. in Böhm (2004), Chung et al. (2000), Ghosh (2011) and Willoughby et al. (2012) have gained significant popularity. Specifically, the asymptotic theory-based computational homogenization methods, with implicit assumptions of macroscopic homogeneity and microscopic periodicity have found extensive applications (Ghosh, 2011; Fish and Shek, 2000; Ghosh et al., 1995; 1996; Guedes and Kikuchi, 1991; Kouznetsova et al., 2002; Terada and Kikuchi, 2000). Analogously, the FE^2 multi-scale methods (Feyel and Chaboche, 2000) also solve micro-mechanical RVE models for every element integration point to obtain homogenized properties. Uncoupling of governing equations at different scales is commonly achieved through the incorporation of mathematically convenient pre-determined boundary conditions like uniform displacement, periodicity on the RVEs.

Introduced in Hill (1963), the representative volume element or RVE is identified as a characteristic representation of the microstructure through which the effective properties of the material can be evaluated without having to solve the entire mi-

* Corresponding author.
E-mail address: sghosh20@jhu.edu (S. Ghosh).

http://dx.doi.org/10.1016/j.ijsolstr.2017.02.015
0020-7683/

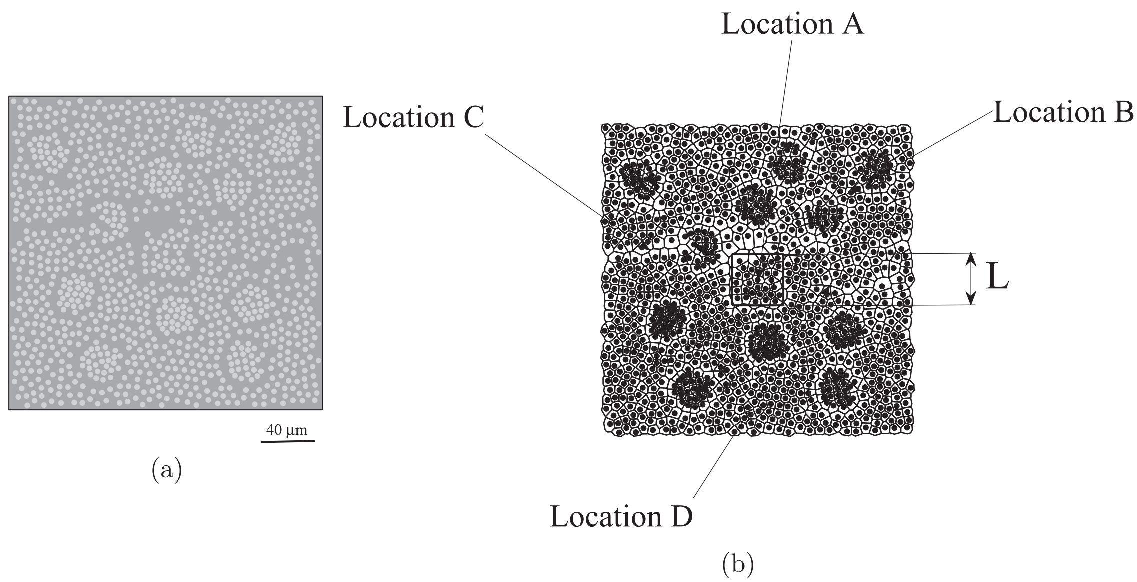

Fig. 1. (a) Micrograph of a clustered microstructure and (b) microstructure tessellated into Voronoi cells showing regions of potential microstructural SERVE.

crostructural region. This RVE concept has been often used for the evaluation of effective properties e.g. in Stroeven et al. (2004), Thomas et al. (2008) and Heinrich et al. (2012). In this context, simplified RVEs consisting of unit cell models are popular (Zeman and Sejnoha, 2007). They assume that underlying heterogeneous microstructure can be characterized by a periodic repetition of the unit cell and typically periodic boundary conditions are applied to solve the microstructural unit cell problem. For many practical cases however, real composite microstructures comprise non-uniformly dispersed heterogeneities with clusters and matrix rich regions (Shan and Gokhale, 2002). This is shown in the micrograph of a unidirectional composite in Fig. 1(a), which cannot be represented by a simple periodic repetition of an unit cell. The concept of statistically representative RVE or SERVE has been proposed in Swaminathan et al. (2006a); 2006b) and Ghosh (2011) using statistical and computational analyses for non-uniformly distributed microstructures. In this development a SERVE has been defined as the smallest volume of the microstructure that satisfies the following characteristics:

1. Effective material properties in the SERVE should be equivalent to those of the entire microstructure. This can be further classified as a property based SERVE or P-SERVE.
2. Distribution functions of parameters reflecting the local morphology in the SERVE should be equivalent to those for the overall microstructure. This can be further classified as a microstructure-based SERVE or M-SERVE.
3. The SERVE should be independent of location in the local microstructure (A,B,C, D in Fig. 1(b)), as well as the applied loading.

Fig. 1(b) shows a computer-generated image of the optical micrograph in Fig. 1(a) that is tessellated into a network of Voronoi cells following methods described in Ghosh (2011). The square region of dimension L is used to identify N characteristic inclusions that constitute a SERVE. An optimal SERVE size is important to avoid either risking erroneous estimation of effective properties with smaller RVE sizes, or requiring exorbitant computational resources with larger that required RVEs. Various statistical descriptors have been used to estimate the volume of the microstructure that needs to be sampled for obtaining the homogenized properties representing bulk material response and hence the SERVE size. These descriptors typically include distributions of the local fiber-volume-fraction, nearest-neighbor-distance, radial-basis-functions and n-point correlation functions. Important contributions have been made in Everett (1993), Pyrz (1994), Torquato (1997), Zeman and Sejnoha (2007), Kanit et al. (2003), Al-Ostaz et al. (2007), Wilding and Fullwood (2011), Zangenberg et al. (2012), Romanov et al. (2013), Guo et al. (2014), Liu and Ghoshal (2014), Bednarcyk et al. (2015) and Liu and Shapiro (2015). The n-point correlation functions have been introduced in Jiao et al. (2007a), Jiao et al. (2007b), Tewari et al. (2004), Fullwood et al. (2008) and Niezgoda et al. (2008); 2010) to reconstruct the microstructure and obtain homogenized properties.

Methods of RVE determination, in most cases, focuses only on the evaluation of the volume and material content and distribution in the microstructure. No consideration is generally given to the appropriateness of the *boundary conditions* for solving the RVE micromechanics problem in the homogenization process. Conventionally, three types of boundary conditions are applied on the RVE. These are:

1. Affine transformation based displacement boundary condition (ATDBC), expressed as:

   $$u_i^A = \epsilon_{ij}^0 x_j \text{ on } \Gamma_{RVE}$$

   Here ϵ_{ij}^0 is a constant applied far-field strain and x_j are the boundary positions, measured from the geometrical centroid of the RVE.
2. Uniform traction boundary condition (UTBC) given as:

   $$T_i = \sigma_{ij}^0 n_j \quad \text{on } \Gamma_{RVE}$$

   T_i is the applied traction on the RVE boundary resulting in a constant stress σ_{ij}^0, where n_j is the unit normal to the RVE boundary.
3. Periodic boundary condition (PBC), expressed as:

   $$u_i^P = \epsilon_{ij}^0 x_j + u_i^{pd} \quad \text{on } \Gamma_{RVE}$$

   The periodic additional displacement u_i^{pd} is equal on opposite faces of the RVE, which requires the boundary to be homologous.

The uniform strain condition provides the lower bound or Voigt bound, while the uniform traction case gives the upper bound or Reuss bound. The underlying assumption of the ATDBC and UTBC is that strains and stresses immediately outside the simulated RVE is constant. Effects of subjecting RVEs to either constant-strain or constant-stress boundary conditions have been studied in Hazanov and Huet (1994), Zohdi and Wriggers (2004) and Ostoja-Starzewski (2007). These boundary conditions assume that the RVE is immersed in a continuum (exterior to the RVE) whose strain-energy-density is spatially invariant and ignore the presence and interaction effects of fibers exterior to the RVE. The periodic boundary condition, on the other hand, assumes the deformation patterns in the domain exterior to the RVE to be homologous. However for composites with non-uniform distributions, the above assumptions of strain energy invariance or periodicity are invalid in the vicinity of the RVE boundary. All of these boundary conditions can result in an over-estimation of the RVE region due to convergence requirements. It is necessary to prescribe appropriate boundary conditions that reflect the actual microstructural statistics.

In a recent paper (Ghosh and Kubair, 2016), the authors have addressed the above limitations of boundary conditions have been overcome by prescribing exterior statistics-based boundary conditions or *ESBCs*. ESBCs represent boundary conditions that reflect the effect of the region exterior to the SERVE domain on the interior. By prescribing ESBCs that incorporate the statistics of the exterior microstructure on the SERVE boundaries, a significant reduction is achieved in the volume of the converged SERVE. Excellent convergence rates have been observed for elastic stiffness components in comparison with the other boundary conditions above, and also with statistical volume elements or SVE's. The study in Ghosh and Kubair (2016) was however for statistically homogeneous distributions only, and did not consider regions of clustering or matrix rich regions as shown in Fig. 1. Correspondingly the distance-based two-point correlation functions or radial distribution functions were sufficient to represent the statistics of the exterior region for these composites. Microstructures with near-identical radial distance-based two-point correlation functions are termed as homometric structures or homomorphs (Patterson, 1939; 1943).

This present paper extends the above study of SERVEs with exterior statistics-based boundary conditions (ESBCs) to statistically nonhomogeneous composite microstructures with clustered and matrix-rich regions. For these morphologies, the radial distribution function is no longer sufficient to differentiate between clustered and unclustered microstructures due to the lack of orientation information in the statistical functions (Patterson, 1939; 1943; Yeong and Torquato, 1998; Rozman and Utz, 2002; Gommes et al., 2012). Hence, ESBCs using this function are unable to represent the effect of the true dispersions in the exterior microstructure. This shortcoming is overcome in this paper through the successful introduction of a joint, radial and angular distance-based two-point correlation function in the ESBCs.

Section 2 summarizes the method of development of the exterior statistics-based boundary conditions (ESBC) for SERVEs and their computational implementation. The development of statistical functions for describing nonhomogeneous microstructures is discussed in Section 3. Validation tests of the ESBCs on the SERVE domain are conducted in Section 4, and the selection process for a candidate SERVE is discussed in Section 5. In Section 6, the performance of a SERVE with ESBC is compared with the statistical volume elements (SVE) approach. The paper concludes with a summary in Section 7. The nomenclature for various terms are given below.

Nomenclature

RVE	Representative volume element
SERVE	Statistically equivalent representative volume element
MVE	Microstructural volume element
SVE	Statistical volume elements
ESBC	Exterior statistics-based boundary condition
ATDBC	Affine transformation-based displacement boundary condition
UTBC	Uniform traction boundary condition
PBC	Periodic boundary condition
SIGF	Statistically informed Green's function

2. Exterior statistics based boundary conditions for the SERVE problem

A summary of the development of the exterior statistics based boundary conditions is given in this section, while details are provided in Ghosh and Kubair (2016). The microstructural volume element or MVE corresponding to a macroscopic point, for which a homogenized property is sought, occupies a locally infinite region $\Omega^{mve} \to \Omega^{\infty}$ as depicted in Fig. 2(a). The MVE consists of nonuniformly dispersed heterogeneities, e.g. fibers, particulates etc. with clusters and matrix rich regions as shown in Fig. 1(a).

The homogenized constitutive response of a linear elastic MVE occupying a domain Ω^{mve} is written as:

$$\bar{\sigma}_{ij}^{mve} = \bar{C}_{ijkl}^{mve}\bar{\epsilon}_{kl}^{mve} \tag{1}$$

where $\bar{C}_{ijkl}^{mve}$ is the homogenized stiffness tensor, and $\bar{\sigma}_{ij}^{mve}$ and $\bar{\epsilon}_{ij}^{mve}$ are the homogenized stress and strains which may be expressed as:

$$\bar{\sigma}_{ij}^{mve} = \frac{1}{\Omega^{mve}}\int_{\Omega^{mve}} \sigma_{ij}^{mve}(\mathbf{x})d\Omega \quad \text{and} \quad \bar{\epsilon}_{ij}^{mve} = \frac{1}{\Omega^{mve}}\int_{\Omega^{mve}} \epsilon_{ij}^{mve}(\mathbf{x})d\Omega \tag{2}$$

$\sigma_{ij}^{mve}(\mathbf{x})$ and $\epsilon_{ij}^{mve}(\mathbf{x})$ are the spatially varying microscopic stresses and strains in the MVE. In a finite element formulation of the microstructural problem, the weak form corresponding to the principle of virtual work form of the MVE is written as:

$$\int_{\Omega^{mve}} \sigma_{ij}^{mve}(\mathbf{x})\delta\epsilon_{ij}^{mve}(\mathbf{x})d\Omega = 0 \tag{3}$$

subject to the affine transformation based displacement boundary condition:

$$u_i^A(\mathbf{x}^{\infty}) = \epsilon_{ij}^0 x_j^{\infty} \text{ on } \Gamma^{\infty} \tag{4}$$

where $\delta\epsilon_{ij}$ is the virtual strain, x_j^{∞} are the coordinates of a point on the MVE boundary Γ^{∞} relative to a reference point, such as the centroid of Ω^{mve}. The solution of the weak form (3) for the entire microstructural volume element, typically consisting of a large population of heterogeneities, is computationally prohibitive. To avert this, only a subset of the MVE domain with explicit representation of dispersed heterogeneities, is identified as the SERVE for detailed micromechanical analyses. A candidate SERVE is highlighted in Fig. 2(a). This domain should be optimally small to make it computationally tractable. Thus the ratio of the length scales of the MVE (L^{mve}) to that of the SERVE (L^{serve}) should be sufficiently large, i.e. $\frac{L^{mve}}{L^{serve}} >> 1$.

For reducing the MVE boundary value problem in Eq. (3) to that of the SERVE, the MVE domain Ω^{mve} is partitioned into two complementary domains, viz. the SERVE domain Ω^{serve} and a domain Ω^{ext} exterior to it, i.e. $\Omega^{mve} = \Omega^{ext} \cup \Omega^{serve}$. The effect of the exterior domain Ω^{ext} is manifested through equivalent conditions on

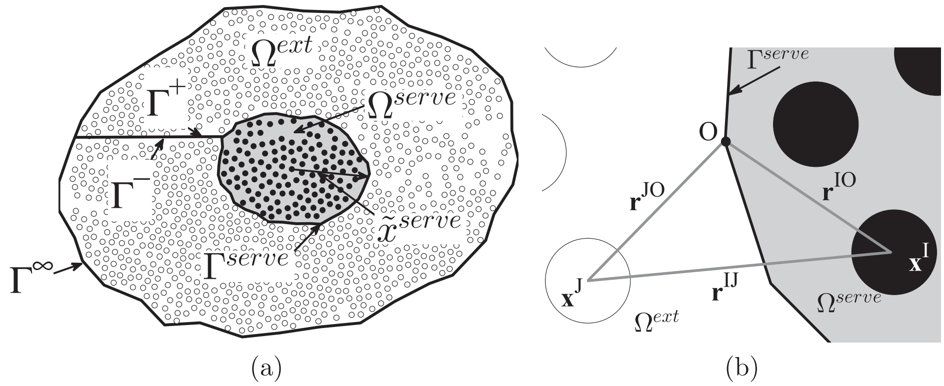

Fig. 2. (a) Schematic view of the MVE containing the SERVE and its complementary exterior domain, i.e. $\Omega^{mve} = \Omega^{serve} \cup \Omega^{ext}$, and (b) effect of an interacting fiber-pair $I - J$ on a field point O at the SERVE boundary Γ^{serve}.

the SERVE boundary Γ^{serve}, adequately reflecting the interaction of Ω^{ext} with Ω^{serve}. It should result in the same invariant strain energy for the SERVE as for the entire MVE with the applied affine displacement conditions on Γ^∞. The equation of principle of virtual work (3) is written as the sum the respective virtual work terms in the complementary domains shown in Fig. 2(a) as:

$$\int_{\Omega^{ext}} \sigma_{ij}^{ext}(\mathbf{x})\delta\epsilon_{ij}^{ext}(\mathbf{x})d\Omega + \int_{\Omega^{serve}} \sigma_{ij}^{serve}(\mathbf{x})\delta\epsilon_{ij}^{serve}(\mathbf{x})d\Omega = 0 \tag{5}$$

Applying the divergence theorem to the first term containing the integral over Ω^{ext}, incorporating equilibrium conditions (in the absence of body forces) $\sigma_{ij,j}(\mathbf{x}) = 0$, and with $\bar{\epsilon}_{ij}^{mve} = \epsilon_{ik}^0$ on Γ^∞, the principle of virtual work (5) reduces to that of the SERVE as (Ghosh and Kubair, 2016):

$$\int_{\Omega^{serve}} \sigma_{ij}^{serve}(\mathbf{x})\delta\epsilon_{ij}^{serve}(\mathbf{x})d\Omega - \int_{\Gamma^{serve}} T_i^{ext}(\mathbf{x})\delta u_i^{ext}(\mathbf{x})d\Gamma = 0 \tag{6}$$

$T_i^{ext}(\mathbf{x})$ is the traction on Γ^{serve} resulting from the stresses in the domain Ω^{ext} exterior to the SERVE. The second term in Eq. (6) will drop out if an effective displacement field can be prescribed on Γ^{serve}, since $\delta u_i^{ext} = 0$ on Γ^{serve}. This can be incorporated through the augmentation of the affine transformation-based boundary displacement field $u_i^A(\mathbf{x}^{serve}) = \epsilon_{il}^0 x^{serve}$ by an additional perturbation term, which represents the effects of heterogeneities in Ω^{ext} on Γ^{serve}. Since the solution process will not involve an explicit numerical solution of the exterior domain problem in Ω^{ext}, a special analytical solution that involves the statistics of the exterior domain can be developed. Hence the term exterior statistics-based boundary conditions or u_i^{ESBC}, that is expressed as:

$$u_i^{ESBC}(\mathbf{x}^{serve}) = u_i^A(\mathbf{x}^{serve}) + u_i^*(\mathbf{x}^{serve}) \text{ on } \Gamma^{serve} \tag{7}$$

where u_i^* is an enhancement due to the interaction of the nonuniform exterior domain Ω^{ext} with the SERVE.

Among a plethora of statistical functions, the $n - point$ correlation functions for characterizing multivariate point sets have been shown to effectively describe arbitrary distributions in Torquato (1997) and Jiao et al. (2007a). In Torquato (2002), it is shown that the spatial statistics of a two-phase medium can be satisfactorily described by the two-point correlation function $S_2(r^{IJ}, \theta^{IJ})$, defined as the probability that two points at positions $\mathbf{x}^I$ and $\mathbf{x}^I$ and separated by a distance r^{IJ} at an orientation θ^{IJ} lie in the same phase α. S_2 is able to characterize anisotropy due to its dependence on the orientation. This is also termed as the joint, distance and orientation-based two-point correlation function. With location-dependent indicator functions for the matrix phase M and I^{th} inclusion phase F_I among n_p inclusions, expressed as:

$$\iota^M(\mathbf{x}) = \begin{cases} 1 & \forall\, \mathbf{x} \in \Omega^M \\ 0 & \forall\, \mathbf{x} \notin \Omega^M \end{cases} \text{ and } \iota^{F_I}(\mathbf{x}) = \begin{cases} 1 & \forall\, \mathbf{x} \in \Omega^{F_I} \\ 0 & \forall\, \mathbf{x} \notin \Omega^{F_I} \end{cases} \quad I = 1 \cdots n_p \tag{8}$$

the joint distance and orientation-based two-point correlation function for Ω^{mve} can be defined as:

$$S_2(\mathbf{r}) = \frac{1}{\Omega^{mve}} \int_{\Omega^{mve}} \iota^F(\mathbf{x})\iota^F(\mathbf{x} + \mathbf{r})d\Omega \tag{9}$$

where $\mathbf{r} = \mathbf{x} - \mathbf{x}^I$ is the position vector separating two points in the domain. This can be represented in a parametric form as (r, θ), where the parameter $r = |\mathbf{r}|$ is the separation distance and $\theta = \angle\mathbf{r}$ is the orientation of the line joining these points with a reference direction. In composites containing equi-radius fibers, the centroids can represent these points. For isotropic distributions, this correlation function reduces to a distance-based, radial distribution function $S_2(r)$. The one-point correlation function, which corresponds to the volume fraction, is expressed as:

$$S_1 = \frac{1}{\Omega^{mve}} \int_{\Omega^{mve}} \iota^F(\mathbf{x})d\Omega \tag{10}$$

The displacements u_i^{ESBC} on the SERVE boundary for heterogeneous microstructures containing inclusion clusters and matrix rich regions are discussed in the following section.

2.1. Exterior statistics based perturbed fields

The presence of heterogeneities in the form of inclusions or fibers alters the spatially invariant, homogeneous state of the matrix stress σ_{ij}^M, strain ϵ_{ij}^M and displacement u_i^M fields in the MVE domain Ω^{mve}. The perturbed stress σ_{ij}^*, strain ϵ_{ij}^* and displacement u_i^* fields depend on the morphological characteristics of the microstructure, e.g. inclusion geometry and location. The total stress σ_{ij}, strain ϵ_{ij} and displacement u_i fields in the heterogeneous MVE domain may be defined as the sum of the homogeneous and perturbed parts as:

$$\sigma_{ij}(\mathbf{x}) = \sigma_{ij}^M + \sigma_{ij}^*(\mathbf{x}), \quad \epsilon_{ij}(\mathbf{x}) = \epsilon_{ij}^M + \epsilon_{ij}^*(\mathbf{x}),$$
$$u_i(\mathbf{x}) = u_i^M + u_i^*(\mathbf{x}) \quad \in \quad \Omega^{mve} \tag{11}$$

Since the homogeneous stress σ_{ij}^M is divergence-free, the equilibrium condition for the perturbed stress fields (in the absence of body forces) is $\sigma_{ij,j}^*(\mathbf{x}) = 0$. The solution to the problem of a heterogeneous medium can be simplified by introducing an equivalent inclusion approach, where an eigenstrain $\epsilon_{ij}^\Lambda(\mathbf{x})$ is introduced in the inclusion domain to account for the constraint that the matrix imposes on the inclusion due to autonomous deformation. Correspondingly, the perturbation stress $\sigma^*_{ij}(\mathbf{x}^{F_I})$ inside the inclusion F_I can be written as:

$$\sigma^*_{ij}(\mathbf{x}^{F_I}) = C^M_{ijkl}\left(\epsilon^*_{kl}(\mathbf{x}) + \iota^{F_I}(\mathbf{x})\epsilon^\Lambda_{kl}(\mathbf{x})\right) \tag{12}$$

where C^M_{ijkl} is the elastic stiffness of the matrix material and $\iota^{F_I}(\mathbf{x})$ is the inclusion indicator function, defined in Eq. (8). The eigenstrain $\epsilon^\Lambda_{kl}(\mathbf{x}^{F_I})$ represents the effect of distributed point source on the perturbed solution $u^*_i(\mathbf{x})$, where $\mathbf{x}^{F_I}$ represent the location of any source point in Ω^{F_I}. Using an infinite-space Green's function solution $G_{ij}(\mathbf{x}, \mathbf{x}^{F_I})$, the perturbed displacement field in Ω^{MVE} with n_p dispersed inclusions can be derived as a summed integral

$$u^*_i(\mathbf{x}) = \sum_{I=1}^{n_p} \int_{\Omega^{F_I}} C^M_{klmn} G_{ik,l}(\mathbf{x}, \mathbf{x}^{F_I}) \epsilon^\Lambda_{mn}(\mathbf{x}^{F_I}) d\Omega \tag{13}$$

where the integral over Ω^{F_I} corresponds to the contribution from individual inclusions. The perturbed strains can be derived from Eq. (13) in terms of eigenstrains as:

$$\epsilon^*_{ij}(\mathbf{x}) = \frac{1}{2}\sum_{I=1}^{n_p} \int_{\Omega^{F_I}} C^M_{klmn}\left(G_{ik,lj}\left(\mathbf{x}, \mathbf{x}^{F_I}\right) + G_{jk,lj}\left(\mathbf{x}, \mathbf{x}^{F_I}\right)\right)\epsilon^\Lambda_{mn}\left(\mathbf{x}^{F_I}\right) d\Omega \tag{14}$$

For isotropic, linear elastic matrix materials, the Green's function has been derived in Mura (1987) as:

$$G_{ij}(\mathbf{x}, \mathbf{x}^{F_I}) = \frac{1}{4\pi\mu}\left[\frac{\delta_{ij}}{r^I} - \frac{1}{4(1-\nu)} r^I_{,ij}\right] \tag{15}$$

where $r^I = |\mathbf{x} - \mathbf{x}^{F_I}|$ is the separation distance between a source point $\mathbf{x}^{F_I}$ and a generic field point $\mathbf{x}$.

Closed form expressions for the integrals in Eqs. (13) and (14) have been derived using elliptic integrals (Eshelby, 1957) with spatially invariant eigenstrains inside ellipsoidal inclusions. The perturbed strains due to any isolated (non-interacting) inclusion F_I in the MVE is expressed as:

$$\epsilon^*_{ij}(\mathbf{x}) = \int_{\Omega^{mve}} H_{ijkl}\left(\mathbf{x}, \hat{\mathbf{x}}\right)\epsilon^\Lambda_{kl}\left(\hat{\mathbf{x}}\right) d\hat{\mathbf{x}} \tag{16}$$

where $\hat{\mathbf{x}}$ is a point in the inclusion. H_{ijkl} corresponds to a unified two-point Eshelby tensor given as:

$$H_{ijkl}\left(\mathbf{x}, \hat{\mathbf{x}}\right) = \iota^{F_I}(\mathbf{x}) S^{F_I}_{ijkl} + \left(1 - \iota^{F_I}(\mathbf{x})\right)\hat{G}^{F_I}_{ijkl}\left(\mathbf{x}, \hat{\mathbf{x}}\right) \tag{17}$$

where $S^{F_I}_{ijkl}$ and $\hat{G}^{F_I}_{ijkl}\left(\mathbf{x}, \hat{\mathbf{x}}\right)$ are the interior and exterior Eshelby tensors. The corresponding perturbed displacements may be written in terms of the Eshelby tensors as:

$$u^*_i(\mathbf{x}) = \int_{\Omega^{mve}} L_{ikl}\left(\mathbf{x}, \hat{\mathbf{x}}\right)\epsilon^\Lambda_{kl}\left(\hat{\mathbf{x}}\right) d\hat{\mathbf{x}} \tag{18}$$

where

$$L_{ikl}\left(\mathbf{x}, \hat{\mathbf{x}}\right) = \iota^{F_I}(\mathbf{x}) T^{F_I}_{ikl}\left(\mathbf{x}, \hat{\mathbf{x}}\right) + \left(1 - \iota^{F_I}(\mathbf{x})\right) D^{F_I}_{ikl}\left(\mathbf{x}, \hat{\mathbf{x}}\right) \tag{19}$$

Expression for the interior and exterior Eshelby tensors $S^{F_I}_{ijkl}$ and $\hat{G}^{F_I}_{ijkl}\left(\mathbf{x}, \hat{\mathbf{x}}\right)$, as well as the displacement-transfer tensors $T^{F_I}_{ikl}\left(\mathbf{x}, \hat{\mathbf{x}}\right)$ and $D^{F_I}_{ikl}\left(\mathbf{x}, \hat{\mathbf{x}}\right)$ for a circular cylindrical fiber are given in the Appendix. For identical fibers in Ω^{mve}, the following reductions hold:

$$S^{F_I}_{ijkl} = S^{F_J}_{ijkl} = S_{ijkl}$$

$$M_{ijkl}\left(\mathbf{x}^I\right) = M_{ijkl}\left(\mathbf{x}^J\right) = M_{ijkl}$$

$$\hat{G}^{F_I}_{ijkl}(\mathbf{r}) = \hat{G}^{F_J}_{ijkl}(\mathbf{r}) = \hat{G}_{ijkl}(r, \theta)$$

where S_{ijkl} and M_{ijkl} are spatially invariant and $\hat{G}_{ijkl}$ is position dependent and describes interactions between the fibers.

The perturbed strain in an inclusion is influenced by its interactions with other inclusions in the MVE. For a population of inclusions represented by the two-point probability distribution function $S_2(\mathbf{r})$ in Eq. (8), the perturbed strain in the fiber F_I, $(I = 1 \cdots n_p)$ due to the interactions of fibers dispersed in Ω^{mve} can be expressed as:

$$\epsilon^*_{ij}\left(\mathbf{x}^{F_I}\right) = S_{ijkl}(\mathbf{x}^I)\epsilon^\Lambda_{ij}\left(\mathbf{x}^I\right) + \int_{\Omega^{mve}\setminus\Omega^{F_I}} S_2(\mathbf{r})\hat{G}_{ijkl}(\mathbf{r})\epsilon^\Lambda_{ij}(\mathbf{r}) d\Omega \tag{20}$$

where $S_2(\mathbf{r})$ is the two-point correlation function defined in Eq. (9). The second integral term represents the interaction effect of all fibers with the I^{th} fiber and the integrand may be denoted as a statistically informed Green's function or SIGF.

The eigenstrains with n_p interacting inclusions are evaluated by applying the Eshelby's stress consistency condition, which requires the total stress inside the fiber Ω^{F_I} to be equal to the total stress in the equivalent matrix domain. For the domain Ω^{mve} consisting of interacting fibers with a distribution represented by the 2-point correlation function $S_2(\mathbf{r})$, the eigenstrain ϵ^Λ_{ij} in a reference fiber occupying a domain Ω^F may be derived using Eq. (12) as:

$$\begin{aligned}\epsilon^\Lambda_{ij}(\mathbf{x}) = &\Bigg[\iota^F(\mathbf{x})\left(S_{ijab} + M_{ijab}\right) - \int_{\Omega^{mve}\setminus\Omega_F} S_2(\mathbf{r})\hat{G}_{ijmn}(\mathbf{r}) \\ &\times \left(S_{mnpq} + M_{mnpq}\right)^{-1}\hat{G}_{pqab}(\mathbf{r}) d\Omega\Bigg]^{-1} \\ &\Bigg[\left(\left(S_{abmn} + M_{abmn}\right)^{-1}\int_{\Omega^{mve}\setminus\Omega_F} S_2(\mathbf{r})\hat{G}_{mnkl}(\mathbf{r}) d\Omega\right) \\ &-\tfrac{1}{2}\left(\delta_{ak}\delta_{bl} + \delta_{al}\delta_{bk}\right)\Bigg]\epsilon^M_{kl} \\ = &A_{ijkl}(\mathbf{x})\epsilon^M_{kl} \quad \forall \mathbf{x} \in \Omega^{mve}\end{aligned} \tag{21}$$

where $M_{ijkl} = \left(C^{F_I}_{ijpq} - C^M_{ijpq}\right)^{-1} C^M_{pqkl}$, $C^{F_I}_{ijkl}$ is the elastic stiffness of the inclusion material and $\mathbf{r}$ is the distance between a source and field point. The perturbed displacements at an observation point O in Fig. 2(b) can be obtained in terms of the matrix strain ϵ^M_{ij} by substituting Eq. (21) into Eq. (18) as:

$$u^*_i(\mathbf{x}) = \left(\int_{\Omega^{mve}\setminus\Omega_F} S_2\left(\mathbf{r}'\right) L_{imn}\left(\mathbf{r}'\right) A_{mnkl}\left(\mathbf{r}'\right) d\Omega\right)\epsilon^M_{kl} \tag{22}$$

Finally, using Eq. (7), the affine transformation based displacement fields can be superposed on the above perturbed displacements to prescribe the exterior statistics-based boundary conditions (ESBCs).

2.2. Implementation of the exterior statistics-based boundary conditions (ESBCs)

The ESBCs are implemented on the boundary Γ^{serve} of a SERVE domain Ω^{serve} of size L using the following steps.

1. Discretize the SERVE domain Ω^{serve} into a finite element mesh. For the 3D domains considered in this study, 4-noded tetrahedral elements are used.
2. Extract the positions and coordinates x_i of all the boundary-nodes on Γ^{serve}.
3. Compute the affine transformation based displacements $u^A_i(\mathbf{x})$ on all the boundary nodes with the applied far-field strain ϵ^0_{ij} as $u^A_i(\mathbf{x}) = \epsilon^0_{ij} x_j$ where x_j is measured relative to the centroid of the SERVE.

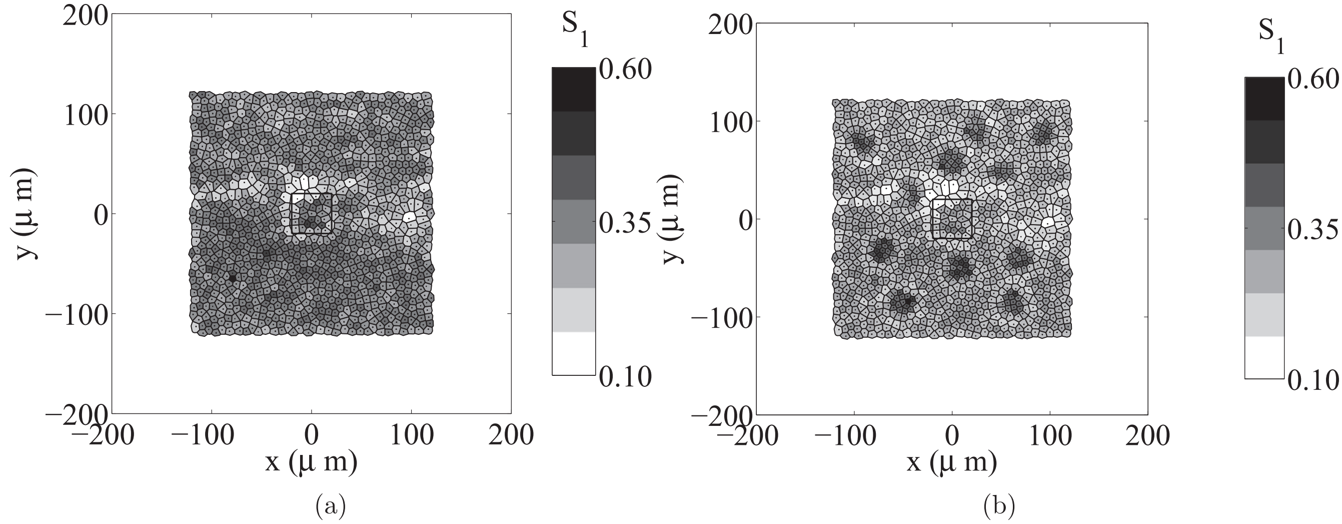

Fig. 3. Microstructural volume elements generated from data provided in Lenthe and Pollock (2014): (a) without-clustering and (b) with clustering. Shading of the Voronoi cells represent the local volume-fraction Φ.

4. Compute the two-point correlation function $S_2(r, \theta)$ for the entire MVE domain Ω^{mve} using Eq. (9).
5. Compute the perturbed displacements u_i^* using Eq. (18) incorporating $S_2(r, \theta)$ for all the boundary nodes, using the following steps.
   - Each radial orientation is discretized into N_r number of equally spaced segments with increment $\Delta r = \frac{R-a}{N_r}$, where a is the radius of the fibers, R is the radius of horizon that corresponds to the extent of the MVE and the lower limit of the integration is $r = a$. The α^{th} radial point is given as $r_\alpha = \alpha \frac{R-a}{N_r}$.
   - The angular orientation is discretized into N_θ equally spaced points of $\Delta\theta = \frac{2\pi}{N_\theta}$. The β^{th} angular point is $\theta_\beta = \beta \frac{2\pi}{N_\theta}$.
   - At a SERVE boundary node at x_i, the discrete perturbed displacement components in Eq. (22) are evaluated for an applied strain ϵ_{ij}^0 as:

$$u_i^*(\mathbf{x}) = \Bigg[\frac{2\pi (R-a)}{N_r N_\theta} \sum_{\alpha=1}^{N_r} \sum_{\beta=1}^{N_\theta} \alpha L_{imn}(\mathbf{x} - (\alpha\Delta r, \beta\Delta\theta)) \quad (23)$$

$$A_{mnkl}(\mathbf{x} - (\alpha\Delta r, \beta\Delta\theta)) S_2(\mathbf{x} - (\alpha\Delta r, \beta\Delta\theta)) \Bigg] \epsilon_{ij}^0$$

6. The ESBCs on the boundary nodes are computed and applied as:

$$u_i^{ESBC}(\mathbf{x}) = u_i^A(\mathbf{x}) + u_i^*(\mathbf{x}) \quad (24)$$

3. Statistical functions for ESBCs in nonhomogeneous microstructures with clustering

In Ghosh and Kubair (2016), ESBCs have been developed for homogenous, non-uniformly distributed microstructures that do not have any dominant clusters or matrix rich regions. For these microstructures, the radial distribution corresponding to a distance-based two-point correlation function $S_2(r)$ is found to be sufficient for representing the microstructural statistics needed for the ESBCs. The sufficiency of this function $S_2(r)$ is however questionable for obtaining ESBCs of clustered and matrix rich microstructures, and is examined in this section.

Fig. 3(a) and (b) show sections of MVEs of unclustered and clustered uniaxial fiber composite microstructures that are tessellated into Voronoi cells, based on fiber centroids. The MVEs described in this study are generated from data on real glass-fiber epoxy-matrix composites that have been characterized in Lenthe and Pollock (2014). The shading of the Voronoi cells represents the local volume-fraction of the fiber in the cells Φ, which is defined as the ratio of the fiber cross-sectional area to the area of the associated Voronoi polygon. Cells with lower values of Φ indicate regions that are matrix rich (brighter), while cells with large Φ are shaded darker, indicating regions of fiber clustering. The relatively homogeneous MVE in Fig. 3(a) has an uniform shading of cells delineating the absence of fiber clustering in the MVE. However, a few bright cells exist, indicating matrix rich regions. The clustered MVE in Fig. 3(b) depicts an increase in Φ due to fiber clustering, illustrated by the darker Voronoi cells, and with spatial non-uniformity of cell shades. In the cluster regions, smaller nearest neighbor distances between fibers leads to stronger fiber interactions causing increased strain and stress concentrations. In the limit, when two fibers touch each other, the stress concentration can reach a stress levels of singularity, necessitating special high fidelity finite element meshes.

The probability density function (PDF) of the local volume fraction Φ are plotted as a function of Φ in Fig. 4(a) for the unclustered (wo-cl) and clustered (w-cl) MVEs. Also, the radial distribution functions $S_2(r)$ in Eq. (9) normalized by the square of the overall volume fraction $S_1(r)$ in Eq. (10) are plotted with respect to the normalized distance r/a in Fig. 4(b). The PDF's of the volume fraction for the clustered and unclustered MVE's are distinguishable. Without clustering, it is uni-modal with a median volume fraction of $\Phi = 0.2513$, while it is bimodal for the clustered microstructure with a second mode near $\Phi = 0.4$ due to the increase in the local volume fractions. The low volume fraction in this study corresponds to that of the real epoxy-matrix glass fiber composite microstructure obtained from data in Lenthe and Pollock (2014). However, the methodology developed for obtaining exterior statistics-based boundary conditions is not restricted to any range of volume fractions. On the other hand, the normalized radial distribution function in Fig. 4(b) for the unclustered and clustered MVEs are almost indistinguishable. Such microstructures with indistinguishable distance-based two-point correlation functions or radial distribution functions are termed as *homomorphs* or *homometric structures* in Patterson (1939); 1943) and Rozman and Utz (2002). This ambiguity has been studied for microstructure reconstruction in Yeong and Torquato (1998) and Gommes et al. (2012). This indistinguishable characteristic of

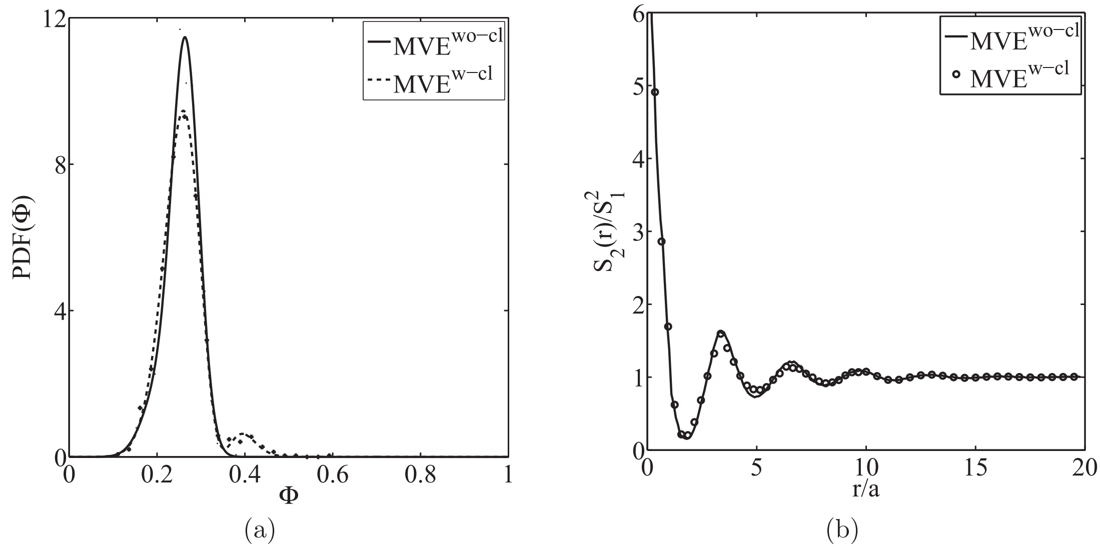

Fig. 4. (a) Probability distribution function of the MVE volume-fraction and (b) normalized distance based two-point correlation of the MVE.

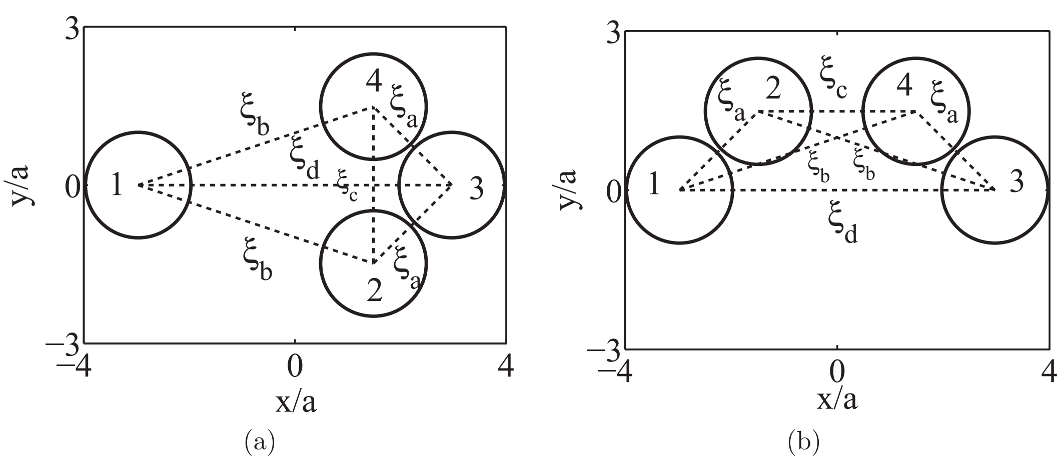

Fig. 5. Homometric microstructures: (a) kite configuration of four fibers, and (b) isosceles trapezoid configuration of four fibers.

distance-based two-point correlation functions makes them inadequate for developing ESBCs on Γ_{SERVE} for non-homogeneous microstructures. This shortcoming can be overcome through the use of joint, distance and orientation-based two-point correlation functions $S_2(r, \theta)$ as discussed in Fullwood et al. (2008) and Niezgoda et al. (2008).

3.1. Two-point correlation functions for unique statistical representation

3.1.1. Tests on simple homometric structures

The effectiveness of the joint, distance and orientation based two-point correlation function $S_2(r, \theta)$ (henceforth termed as joint two-point correlation function) in uniquely describing *homometric microstructures* is illustrated in this section. Two, four-fibered microstructures obtained by cyclotomic sets (Patterson, 1943) are depicted in Fig. 5. The kite microstructure in Fig. 5(a) consists of one cluster of three-fibers, while the isosceles trapezoid microstructure in Fig. 5(b) consists of two clusters of two fibers in each.

A normalized nearest-neighbor distance parameter is defined as $\xi_a = \frac{d_a}{a}$, where d_a is the nearest-neighbor distance and a is the fiber radius. For both the microstructures, $\xi_a = 2 + \eta$, where η is the normalized ligament length between the nearest fiber-pair. When $\eta = 0$ the fibers touch each other, while for large values of η the interaction between the fibers becomes negligible with very low local-volume-fractions. For the kite and isosceles-trapezoidal microstructures in Fig. 5 the normalized ligament length is set to $\eta = 0.05$ to represent clustering. Other inter-fiber distances are identical and are written in terms of ξ_a in Table 1.

Table 1
Inter-fiber distance of the kite (Fig. 5(a)) and isosceles trapezoidal (Fig. 5(b)) microstructures.

Distance indicator (ξ)	$\frac{\xi}{\xi_a}$
ξ_a	1
ξ_b	$\sqrt{5}$
ξ_c	$\sqrt{2}$
ξ_d	$2\sqrt{2}$

The distance-based radial distribution function $S_2(r)$ for the kite and trapezoidal microstructures are identical as depicted in Fig. 6(a). Consequently, the representation of fiber interaction using $S_2(r)$ will lack uniqueness for these homomorphs. The ambiguity is overcome by the joint correlation function $S_2(r, \theta)$ in Eq. (9), where θ is the orientation of the line with respect to a reference direction. The $S_2(r, \theta)$ functions for the kite and trapezoid microstructures in the normalized space are shown in Fig. 6(b) and (c). This function is capable of distinguishing between the microstructures

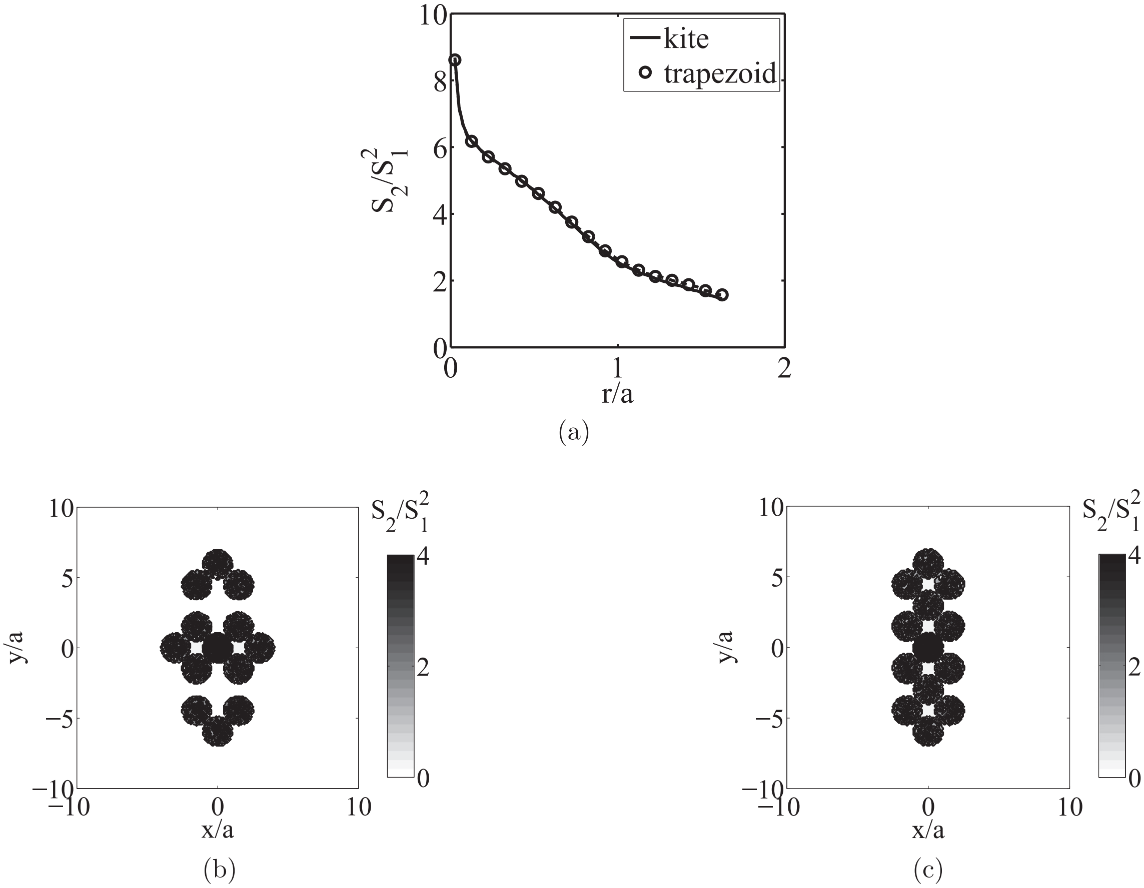

Fig. 6. (a) Normalized radial distribution function of the kite and trapezoid configurations, (b) normalized joint two-point correlation function of the kite configuration (Fig. 5(a)), and (c) normalized joint two-point correlation function of the isosceles-trapezoid configuration (Fig. 5(b)).

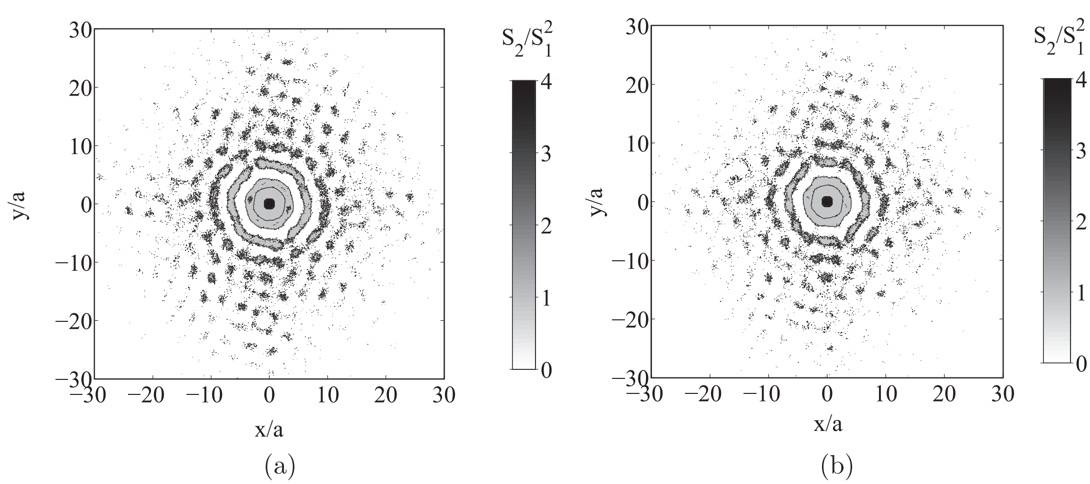

Fig. 7. Joint two-point correlation function of the MVE: (a) without clusters (Fig. 3(a)), and (b) with clusters (Fig. 3(b)).

uniquely, and hence will be used for developing the statistically informed Green's functions in the ESBCs.

3.1.2. Microstructural volume elements (MVEs) with and without clusters

The normalized two-point correlation functions $\frac{S_2(r,\theta)}{S_1^2}$ are plotted for the unclustered and clustered MVEs in Fig. 7(a) and (b). The microstructures, characterized by this function, are uniquely distinct. The probability of finding vectors inside the fibers is maximum near the center, as depicted by the peak. The function oscillates and reaches a far-field value of S_1^2. The difference between $\frac{S_2(r,\theta)}{S_1^2}$ for the unclustered and clustered MVEs are shown in the contour plot of Fig. 8. The difference field clearly demonstrates the orientation dependence due to the addition of microstructural clusters.

The effect of excluding large SERVE sizes from the MVE, on the joint two-point correlation function $S_2(r, \theta)$ of the exterior domain Ω^{ext} is examined next. Statistical functions such as $S_2(r, \theta)$, rep-

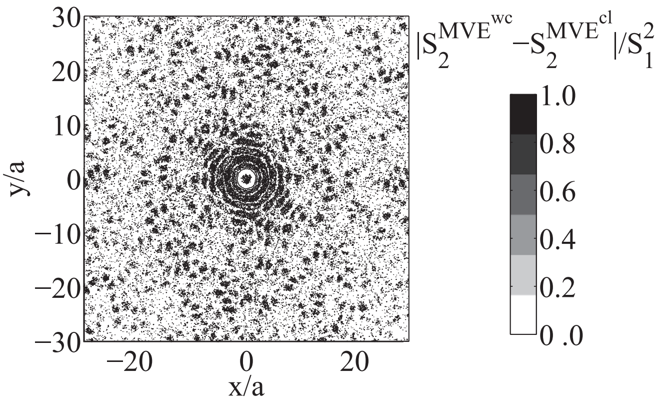

Fig. 8. Difference in the two-point correlation of MVEs without and with clusters.

resenting the characteristics of the microstructure, are necessary for the development of the ESBCs. Generally, these functions are evaluated from experimental characterization of large images obtained e.g. by scanning electron microscopy. This study establishes if there is need to re-evaluate these functions due to the extraction of the SERVE from the parent MVE. A candidate SERVE of size 300 μm × 300 μm that is 10% in size of the Ω^{mve}, is excluded from the MVE and the $\frac{S_2(r,\theta)}{S_1^2}$ function is calculated for the exterior domain. The normalized correlation function for the entire MVE is shown in Fig. 9(a), while that for the 90% exterior domain is shown in Fig. 9(b). The two plots are quite similar. Divergence due to the exclusion of the SERVE occurs only at large distances $r > 10a$, at which distances the fiber interaction is weak. Hence, the two-point correlation function for the Ω^{mve} can be used for that of Ω^{ext} in the evaluation of ESBCs.

4. Verification of ESBCs for SERVEs in non-homogenous microstructures with clustering

The exterior statistics-based boundary conditions (ESBCs) for the SERVE, developed in Section 2.1, are examined for accuracy. Finite element simulations are conducted for a MVE with section size 240 μm × 240 μm × 10 μm and consisting of 1152 fibers with clusters. The fibers have a uniform 4 μm diameter. A candidate SERVE cross-section of 40 μm × 40 μm × 10 μm encompassing 38 fibers, is highlighted by the white square boundary in Fig. 10(a). The computational domains are discretized into meshes of 4-noded tetrahedral elements of a minimum size of 0.8 μm and with 13 elements in the z-direction. The Young's modulus and Poisson's ratio of the epoxy matrix are $E^M = 3.2GPa$ and $\nu^M = 0.4$, while those for the e-glass-fibers are $E^F = 80GPa$ and $\nu^F = 0.25$ respectively. The first set of simulations correspond to the affine transformation-based applied displacement boundary condition $u_i^A = \epsilon_{ij}^0 x_j$, with an applied far-field strain $\epsilon_{11}^0 = 1$.

Contour plots of ϵ_{11} from the finite element solution are shown on the deformed configuration in Fig. 10(a). The strain inside the fibers are smaller than in the matrix due to the larger fiber Young's modulus. The FE displacement solution along the white line are extracted from FE simulations of the MVE. This is compared with the displacement solution $u_i = u_i^A + u_i^*$ used in ESBC, where u_i^* is the perturbed displacement solution from Eq. (24) using the statistically informed Green's function or SIGF approach. The displacement solutions, normalized by the fiber radius, are plotted in Fig. 10(b). The abscissa corresponds to the total length along the sides of the white SERVE boundary. The markers (0–1) corresponds to the bottom edge, (1–2) to the left edge, (2–3) to the top edge and (3–4) to the right edge. Excellent agreement is seen between results of the FE simulations of MVE shown with markers, and the displacements solutions $u_i^A + u_i^*$ shown in solid lines. This provides a verification of the proposed ESBC approach. The SIGF-augmented solutions show that even though the far field strain is $\epsilon_{11}^0 = 1$, the u_2 component is not zero on the white SERVE boundary due to fiber interactions. Thus, affine-transformation-based displacement boundary conditions (ATDBC) or periodic boundary conditions (PBC), directly applied on the SERVE boundary will suffer in terms of accuracy, as will be shown in the following sections.

4.1. Comparing of ESBCs generated by two-point correlation and radial distribution functions

Fig. 11 compares plots the normalized perturbation displacements u_i^*/a generated using the radial distribution function $S_2(r)$ and the two-point correlation function $S_2(r, \theta)$. The abscissa shows the normalized length along the bottom (edge 0–1), right (edge 1–2), top (edge 2–3) and left (edge 3–4) edges of the 40 μm square SERVE in sequence, in Fig. 10. The applied far-field strain ϵ_{11}^0 affects the perturbation displacements in the x_1 direction, but not much in the x_2 direction. The difference in the perturbation displacement alters the ESBCs applied on the SERVE and hence the computed homogenized stiffness $\bar{C}_{ijkl}$.

Furthermore, the effect of ATDBCs and ESBCs using $S_2(r)$ and $S_2(r, \theta)$ on a candidate SERVE of size $L = 40$ μm containing 38 fibers is illustrated in Figs. 12, 13 and 14 respectively. In this paper, the boundaries of the SERVEs Γ^{serve} are assumed not to intersect the inclusions, for the sake of simplicity. However the developed ESBCs are capable of being prescribed on boundaries that intersect inclusions. The plots in Figs. 12(a), 13(a) and 14(a) show the displacement components in the 1 and 2 directions applied as boundary conditions along the four sides of the SERVE boundary. Perturbations in the ESBCs $u_1 = u_1^A + u_1^*$ are pronounced on the right and left edges of Figs. 13(a) and 14(a). While $u_2^A = 0$ for $\epsilon_{11}^0 = 1$ on the boundary, $u_2 = u_2^*$ is non-zero along the edges with the ESBC. Unlike for PBCs, the deformed edges with the ESBCs are not homologic. Contour plots of the strain ϵ_{11} for the different boundary conditions are shown in Figs. 12(b), 13(b) and 14(b). While regions of strain localization are observed for all the boundary conditions, the intensity is less with ESBCs.

The homogenized stiffness for the entire composite MVE $\bar{C}_{ijk}^{mve}$ is evaluated using Eq. (1), together with the averaged stresses from Eq. (2) corresponding to an applied averaged strain. The same stiffness can be obtained from the averaged stresses in the SERVE domain with the applied ESBCs generated by applying the SIGF to the applied averaged strains. Table 2 tabulates the normalized homogenized stiffness $\bar{C}_{1111}/E^M$ from the entire MVE simulations, as well as from simulating a 40 μm SERVE subjected to ATDBC and ESBCs. For the ESBCs, both the radial distribution $S_2(r)$ in Fig. 13(a) and the joint two-point correlation function $S_2(r, \theta)$ in Fig. 14(a) are considered. The homogenized stiffness obtained from the SERVE simulations with the $S_2(r, \theta)$-based ESBCs are the closest to those obtained from entire MVE simulations. This illustrates the excellent desired performance of the applied ESBCs.

The contour plot of the difference in the maximum principal stress obtained by applying the ATDBC and ESBC with $S_2(r, \theta)$ are shown in Fig. 15(a). The difference is pronounced in ligaments between fibers that are in close proximity. The maximum principal stresses are larger with ATDBCs than with ESBCs for the same far-field strain energy density. Analogously, the contour plot of the difference in the maximum principal stress by ESBCs using the $S_2(r)$ and $S_2(r, \theta)$ functions is shown in Fig. 15(b). While the perturbation displacements in Fig. 11 by using the $S_2(r)$ and $S_2(r, \theta)$-based ESBCs are comparable in magnitude, the stresses are significantly different. The $S_2(r, \theta)$-based ESBCs are accurate as they account for the presence of fiber clusters in the exterior domain.

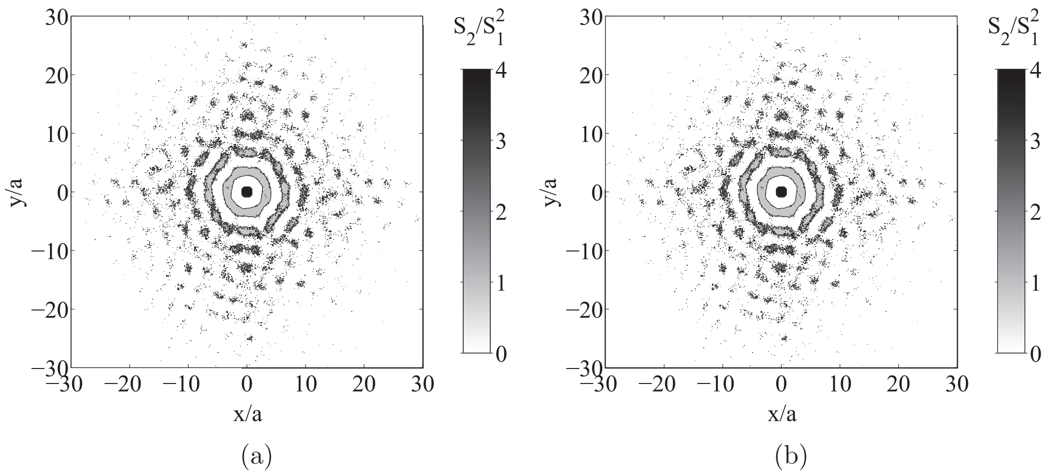

Fig. 9. Joint two-point correlation function of (a) the microstructural volume element Ω^{mve}, (b) the exterior domain Ω^{ext}.

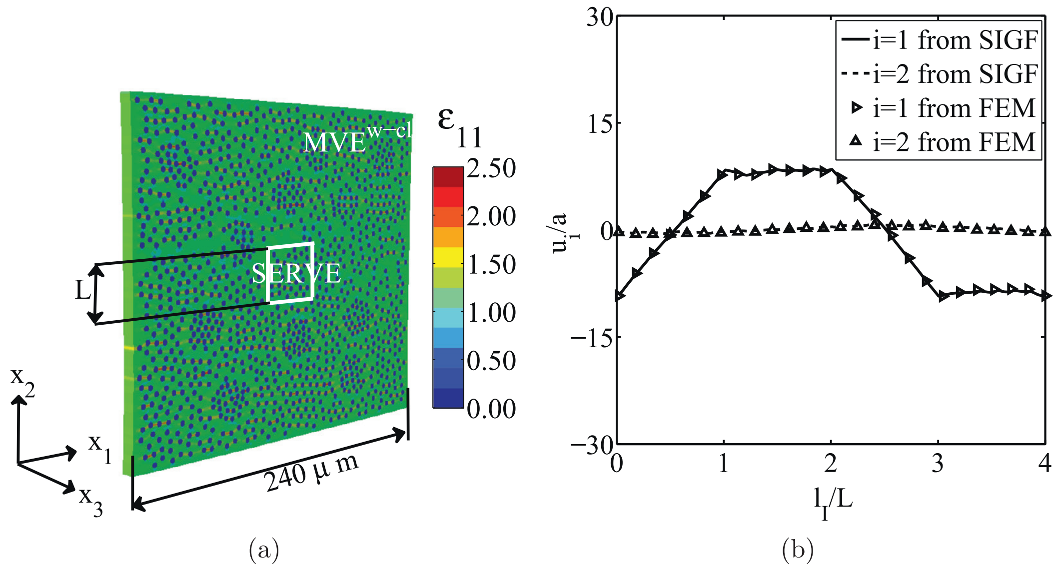

Fig. 10. (a) Contour plot of the FE solution ϵ_{11} in the clustered MVE (obtained from data provided in Lenthe and Pollock (2014)) subjected to a far-field applied strain $\epsilon_{11}^{0} = 1$, (b) comparison of displacements on the 40μm × 40μm SERVE obtained by the SIGF Eq. (24) with that from the finite element simulation of the MVE. (The abscissa marks (0–1) corresponds to the bottom edge, (1–2) to the left edge, (2–3) to the top edge and (3–4) to the right edge of the Γ_{SERVE}.).

Table 2
Homogenized stiffness $\bar{C}_{1111}/E^M$ in SERVEs subjected to different boundary conditions.

Figure	Boundary condition	$\bar{C}_{1111}/E^M$	% error $\left(\frac{\lvert \bar{C}_{1111}^{mve} - \bar{C}_{1111}^{serve} \rvert}{\bar{C}_{1111}^{mve}}\right) \times 100$
(L=240 μm) 10	ATDBC	2.8836	0.0000
12	ATDBC	2.9406	1.9767
13	ESBC using $S_2(r)$	2.9056	0.7620
14	ESBC using $S_2(r, \theta)$	2.8813	0.0798

4.2. SERVEs intersecting clustered regions

For certain microstructural volume elements, it is possible that the SERVE intersects clustered regions in the microstructure. This section examines the effect of prescribing ESBCs on SERVEs that intersect clusters. A 40 μm × 40 μm SERVE intersecting two clusters in the MVE is illustrated in Fig. 16. The MVE depicted in Fig. 16 is the same as that illustrated in Fig. 3(b). The intersection of the clusters with the SERVE boundaries results in a few fibers, belonging to the cluster, to be present inside the SERVE. The fibers that belong to the clusters are highlighted in gray. The prescribed $S_2(r, \theta)$-based ESBCs are shown in Fig. 17(a). The ϵ_{11} strain contour in the SERVE is depicted in Fig. 17(b). Strain concentrations are larger due to the inter-fiber ligaments being reduced due to the fiber clusters. The homogenized stiffness of the SERVE is $\bar{C}_{1111} = 2.8823E^M$, which is almost equal to that obtained from the entire MVE $\bar{C}_{1111}^{\infty} = 2.8836E^M$ as given in Table 2. This example illustrates the effectiveness of the prescribed ESBCs on SERVEs with intersecting clusters.

5. Selection of a candidate SERVE in the MVE and homogenized stiffness convergence

Fig. 18 shows a set of concentric square cross-sections that are candidate SERVEs that can be extracted from the MVE domain. The candidate SERVEs are chosen to consist of an increasing num-

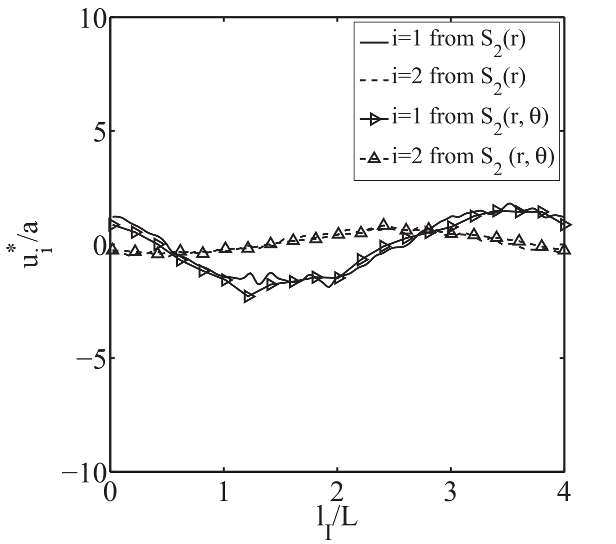

Fig. 11. Perturbation displacements u_i^*/a obtained for a clustered MVE using the $S_2(r)$ and $S_2(r,\theta)$ statistical functions in SIGF.

Table 3
Parameters in the selection of the SERVE.

SERVE	I	II	III	IV	V	VI	VII	MVE
L (μm)	35	40	70	90	124	160	250	300
N_f	13	38	120	176	313	498	1292	1746

ber of fibers. The different SERVE sizes considered are depicted in Fig. 18(i–vii). The thickness of the composite domain is 10 μm. The FE model is discretized into 4-noded tetrahedral elements with 13 elements in the *z*-direction. Details of the SERVE size *L* and the number of fibers N_f enclosed are listed in Table 3.

The candidate SERVEs are subjected to either ATDBCs, PBCs or $S_2(r,\ \theta)$-based ESBCs that corresponds to a far-field unit uniaxial strain $\epsilon_{11}^0 = 1$. All other strain components are kept to zero. Three dimensional finite element simulations of the SERVEs are performed and the homogenized stiffness $\bar{C}_{ijkl},\ i,j,k,l = 1,2,3$ are obtained by post-processing. Details of obtaining the homogenized moduli have been discussed in Swaminathan et al. (2006a). Convergence in the homogenized stiffness with increasing SERVE size is used as a metric to determine the necessary SERVE size. In this study, the dominant stiffness component $\bar{C}_{1111}$ is used to determine the effect of the applied boundary conditions on the converged SERVE size.

The homogenized stiffness component $\bar{C}_{1111}$ is plotted as a function of increasing SERVE size *L* in Fig. 19. In the plots, $L = 0$ corresponds to the matrix alone, for which the SERVE size is a material point of zero volume. The error in Fig. 19(b) is calculated as the difference between the homogenized stiffness component for the SERVEs and that for the entire MVE with *L*=300 μm. Fig. 19(a) clearly shows that the homogenized modulus obtained with the ESBCs converges at a SERVE size of approximately $L = 40$ μm consisting of 38 fibers, as opposed to the much larger SERVE sizes of approximately $L \approx 220$ μm, when subjected to the ATDBC or PBC. The error plots in Fig. 19(b) consolidates this conjecture that convergence with ESBCs is much faster than with the other boundary conditions. This example elucidates the role of exterior statistics on the boundary condition of the SERVE, which is typically ignored with other methods.

Finally, the effect of the two-point correlation functions $S_2(r)$ or $S_2(r,\ \theta)$ used in ESBCs, on the optimal SERVE size is examined. The variation of the volume-averaged stiffness is plotted as a function of the SERVE size in Fig. 20(a). The $S_2(r)$-based ESBCs exhibit much slower convergence leading to larger SERVEs in comparison to SERVEs by the $S_2(r,\ \theta)$-based ESBCs. In the example shown, the SERVE size by the latter boundary condition is less than half of that obtained by the former boundary condition. The plot of error in the homogenized stiffness, shown in Fig. 20(b), also corroborates this conclusion.

6. Comparing the ESBC enhanced SERVE with statistical volume elements (SVEs) for stiffness convergence

Statistical volume elements (SVE) are based on the ergodicity hypothesis that the composite microstructure with dispersed heterogeneities is statistically homogeneous and hence its volume-averages are identical to the ensemble-averages (Yin et al., 2008; McDowell et al., 2011). The homogenized modulus obtained for the MVE is expected to be equal the mean of the volume-averaged

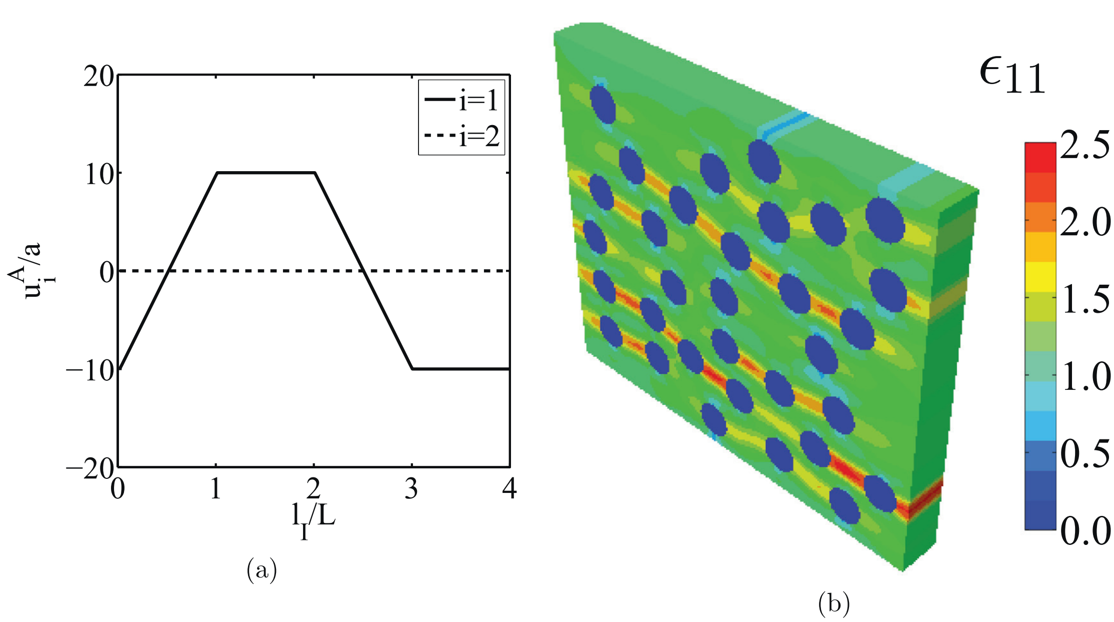

Fig. 12. Results from SERVE simulation with ATDBC: (a) displacements on the boundary of the SERVE, (b) contour plot of ϵ_{11} in the SERVE.

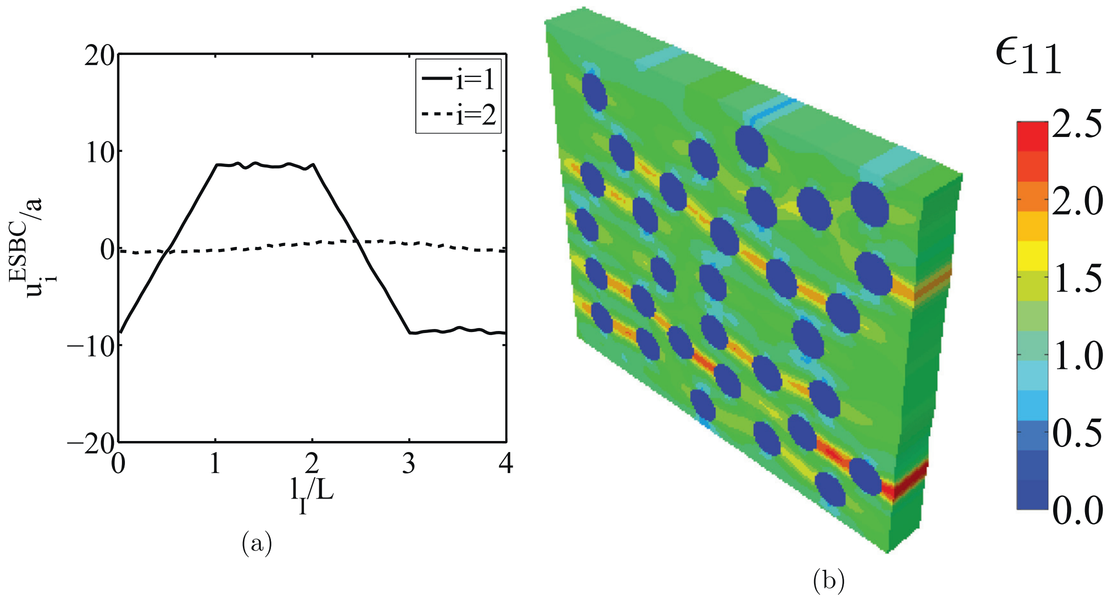

Fig. 13. Results from SERVE simulation with ESBC generated by radial distribution function $S_2(r)$: (a) displacements along the SERVE boundary, (b) contour plot of ϵ_{11} in the SERVE.

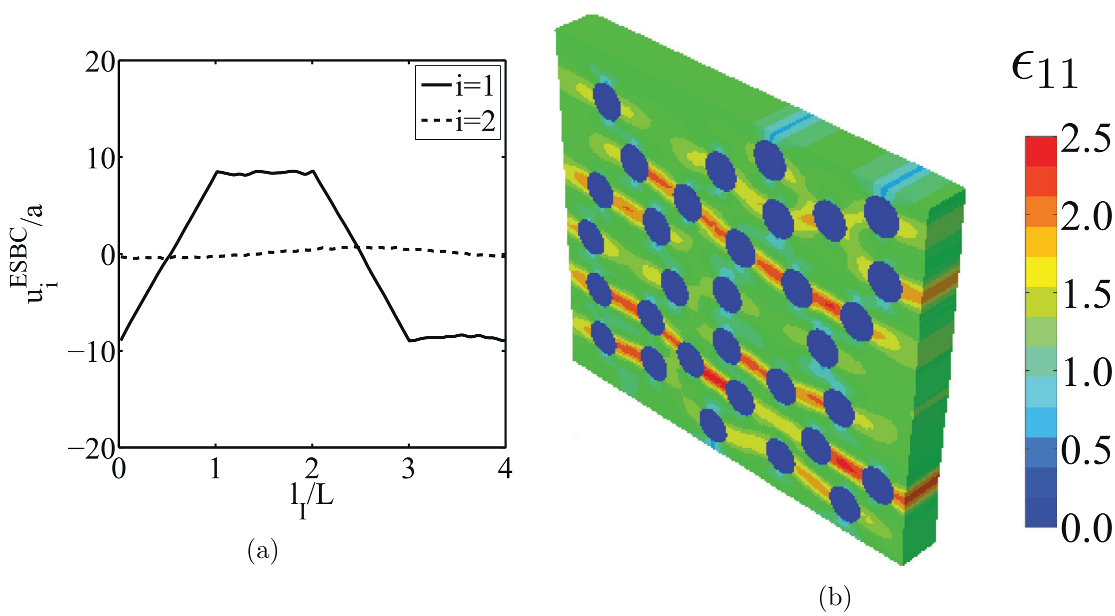

Fig. 14. Results from SERVE simulation with ESBC generated with the two-point correlation function $S_2(r, \theta)$: (a) displacement along the SERVE boundary, (b) contour plot of the ϵ_{11} in the SERVE.

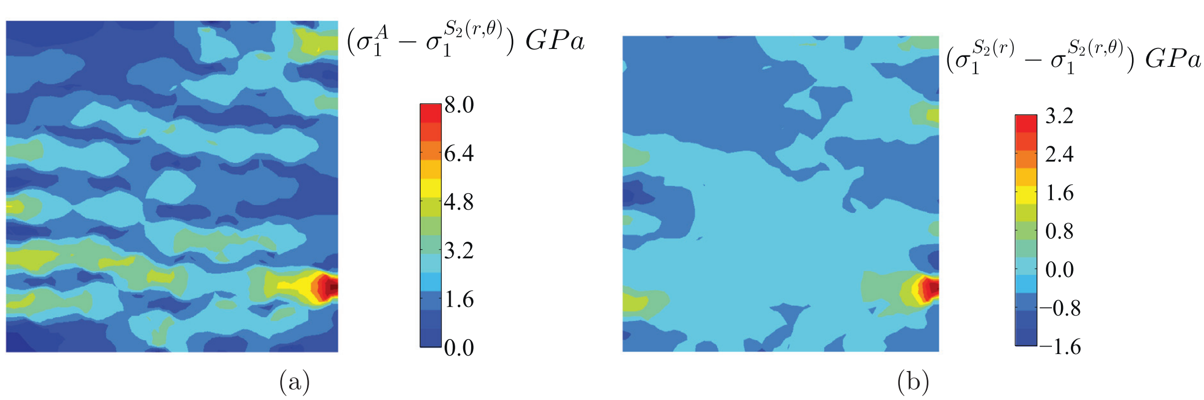

Fig. 15. Contour plot showing the difference in the maximum principal stresses in the SERVE for: (a) ATDBC and ESBC using $S_2(r, \theta)$ (b) ESBCs using $S_2(r)$ and $S_2(r, \theta)$.

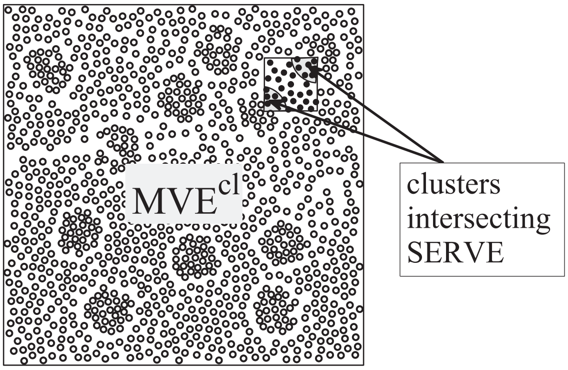

Fig. 16. Intersection of clusters in the MVE with the edges of a SERVE.

modulus obtained from a large number of instantiations of a much smaller analysis volume. The ensemble-average of any spatially varying field quantity $\Psi(\mathbf{x})$ over the SVE may thus be expressed in terms of the homogenized value over the MVE as:

$$\bar{\Psi} = \frac{1}{\Omega^{mve}} \int_{\Omega^{mve}} \Psi(\mathbf{x}) d\Omega = \frac{1}{N} \sum_{I=1}^{I=N} \left(\frac{1}{\Omega^{sve_I}} \int_{\Omega^{sve_I}} \Psi(\mathbf{x}) d\Omega \right), \tag{25}$$

where $\bar{\Psi}$ is the volume-averaged value, Ω^{sve_I} is the domain of the Ith SVE instantiation and N corresponds to the number of sample SVE's in the ensemble. In general, the volume of any SVE is much smaller than that of the RVE, i.e. $\Omega^{sve_I} < \Omega^{rve}$.

For comparison with the SERVE predictions, the SVE problem is set up with individual square SVEs of size $L^I = 60\ \mu$m, 100 μm and 200 μm. 100 candidate SVEs are chosen from the much larger MVE for each SVE size. Two-dimensional plane-strain analysis of the candidate SVEs are performed subjected to ATDBCs and PBCs. The ensemble-averaged stiffness components $\bar{C}_{ijkl}$ are obtained for the population of N SVEs as:

$$\bar{C}_{ijkl} = \frac{1}{N} \sum_{I=1}^{I=N} \bar{C}^I_{ijkl} \tag{26}$$

where $\bar{C}^I_{ijkl}$ are the volume-averaged stiffness components for the Ith SVE. With increasing number of instantiations in the ensemble population N, the ensemble averaged stiffness components are expected to converge to their respective homogenized values for the MVE ($\bar{C}^{\infty}_{ijkl}$). The convergence criterion is defined in terms of the minimum number of instantiations or SVE's N required in the ensemble to attain a steady-state, invariant value of the homogenized stiffness in Eq. (26). Convergence is ascertained from the plot of the cumulative mean (CM) of the normalized stiffness as a function of the ensemble population size N, as shown in Fig. 21(a). The cumulative mean of a stiffness component $\bar{C}_{ijkl}$, normalized by the matrix Young's modulus E^M, is defined as:

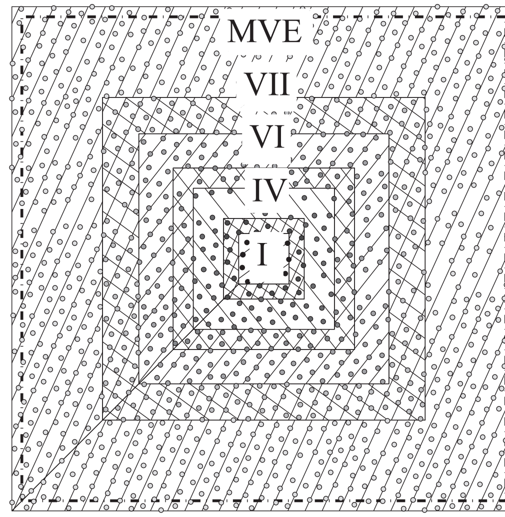

Fig. 18. Concentrically increasing candidate SERVE domains in the MVE generated from data in Lenthe and Pollock (2014).

$$CM\left(\frac{\bar{C}_{ijkl}}{E^M}\right)_N = \frac{1}{N} \sum_{I=1}^{I=N} \frac{\bar{C}^I_{ijkl}}{E^M}$$

For an ergodic microstructure, the cumulative mean (CM) of the volume-averaged stiffness is expected to converge to that of the entire MVE $\bar{C}^{\infty}_{ijkl}$. The CM of $\bar{C}_{1111}$, obtained from the three SVE sizes, are shown in Fig. 21(a). For SVE size $L^{sve} = 60\ \mu$m, the en-

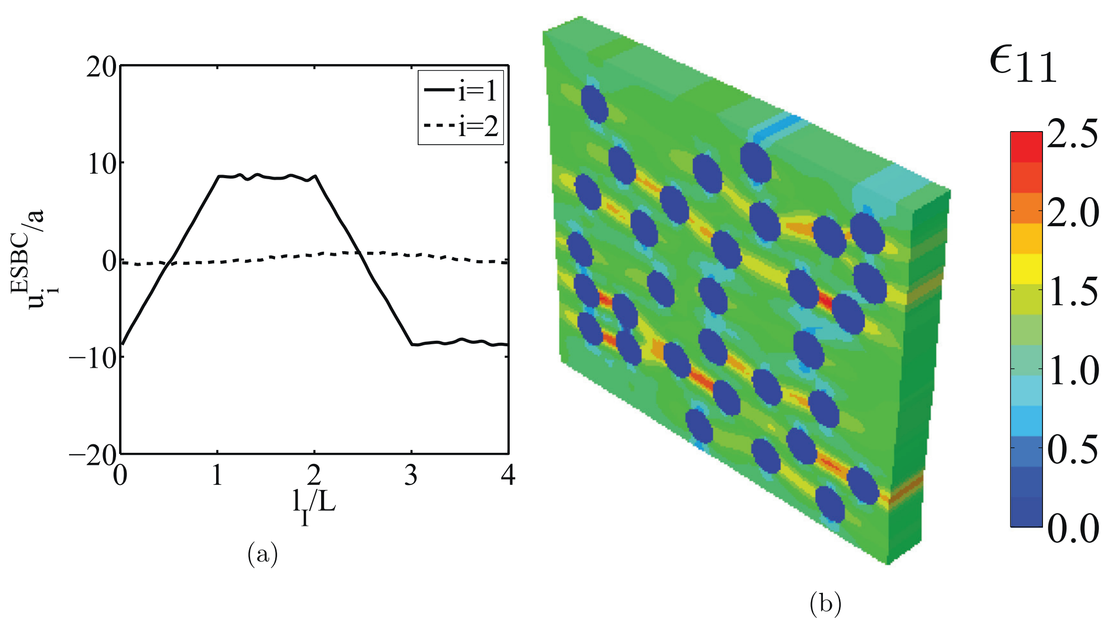

Fig. 17. Results from ESBC from SERVE with edges intersecting clusters: (a) displacement along the SERVE boundary, (b) contour plot of ϵ_{11} in the SERVE.

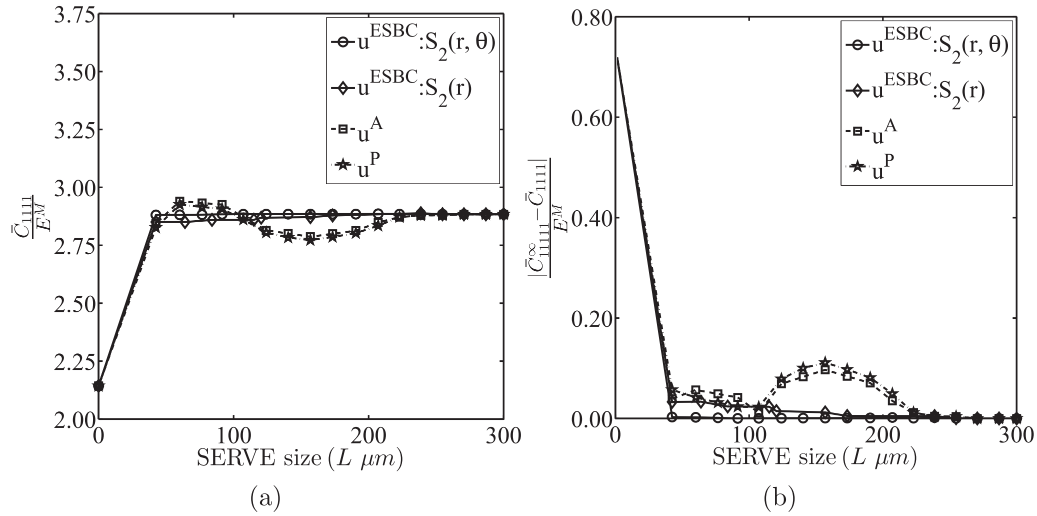

Fig. 19. Variation of: (a) the normalized homogenized stiffness tensor $\bar{C}_{1111}/E^M$, and (b) error in $\bar{C}_{1111}$, as a function of increasing SERVE size.

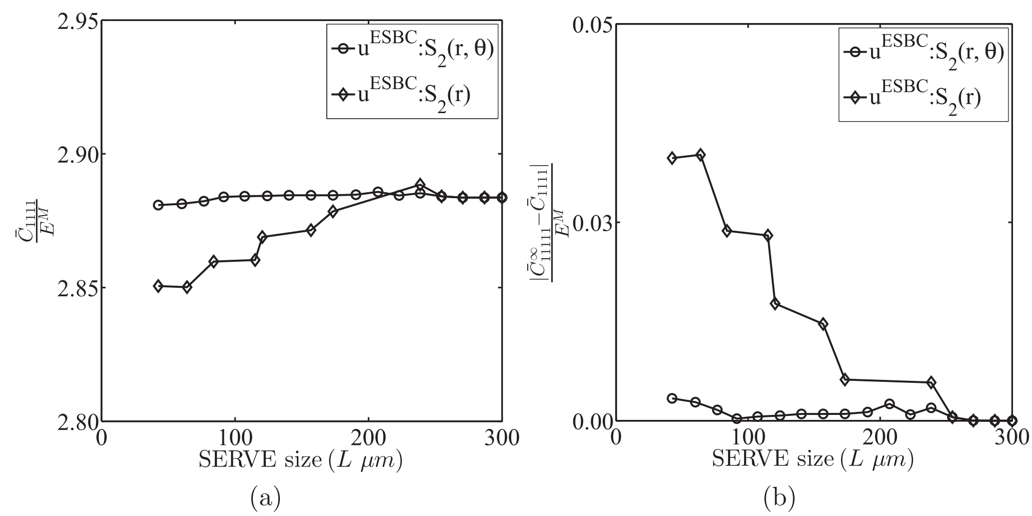

Fig. 20. Convergence of homogenized stiffnesses for $S_2(r)$ and $S_2(r, \theta)$-based ESBCs with increasing SERVE size: (a) variation of the normalized homogenized stiffness tensor $\bar{C}_{1111}/E^M$, and (b) variation of the normalized error.

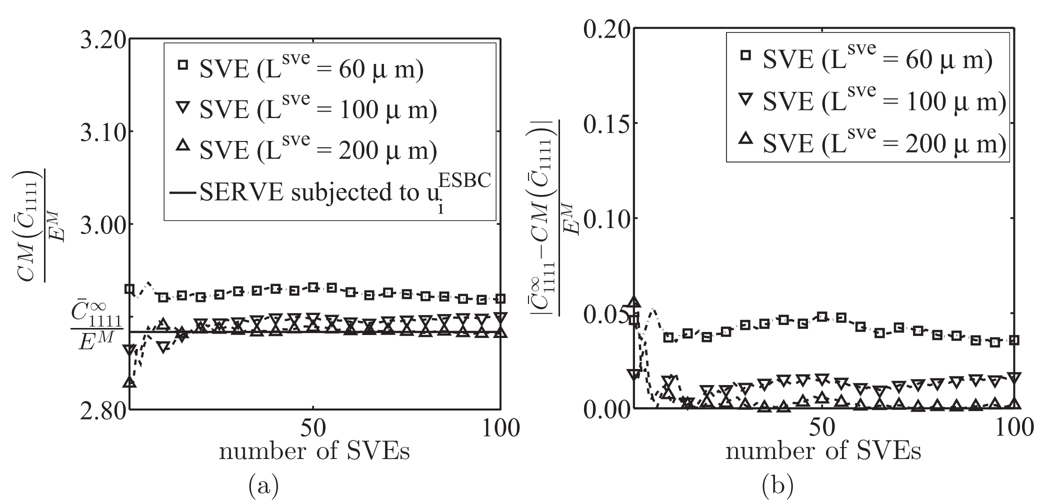

Fig. 21. (a) Cumulative mean (CM) of the ensemble-averaged stiffness component $\bar{C}_{1111}$ as a function of the number of SVEs for different SVE sizes (L^{sve}); (b) error in CM of the stiffness as a function of the number of SVEs.

semble averaged stiffness even with 100 instantiations does not converge to the accurate value obtained from the SERVE analysis as seen. For the SVE size of $L^{sve} = 200$ μm the cumulative-mean converges for ensembles consisting of more than fifteen SVE instantiations. The corresponding error in CM, defined as the difference from the stiffness $\bar{C}^{\infty}_{1111}$, is plotted as a function of the number of SVEs in Fig. 21(b). This exemplifies the lack of convergence in the SVEs of smaller sizes. SERVEs subjected to ESBCs require only one instantiation of size L^{serve} 40 μm for convergence, as illustrated in Fig. 19.

7. Summary and conclusions

This paper has successfully extended the *exterior statistics based boundary conditions (ESBCs)* developed for statistically equivalent RVE's or SERVE's in Ghosh and Kubair (2016), to include non-homogeneous microstructures with clustering and/or matrix-rich regions. The SERVEs, introduced in Swaminathan et al. (2006a); 2006b), are needed for evaluating response functions in nonuniform heterogeneous microstructures. The ESBCs have been originally developed to overcome deficiencies with conventionally applied boundary conditions, such as the affine transformation based displacement boundary conditions (ATDBCs) or periodic boundary conditions (PBCs) in evaluating homogenized material properties. These deficiencies arise from overlooking the actual statistics of heterogeneities in nonuniform microstructures, where the effect of the exterior microstructure on the SERVE can be significant. Typically, these conventional boundary conditions lead to a much larger than required size of the RVE for convergence of homogenized material properties. This comes with significantly higher computational costs for microstructural simulations. The proposed ESBCs have the potential to optimally reduce the converged SERVE size by accounting for the interaction of the heterogeneities in the domain that is exterior to the SERVE in the material microstructure.

ESBCs from small deformation elasticity problems have been obtained in Ghosh and Kubair (2016) by using a statistically informed Green's function (SIGF) method that accurately describes interactions with heterogeneities exterior to the SERVE domain in the microstructure. The SIGF solution employs the Eshelby equivalent inclusion method in accounting for the fiber interactions in a statistical sense. Microstructures considered in Ghosh and Kubair (2016) however were statistically homogeneous with no fiber clustering or matrix rich regions. These are adequately characterized by the distance-based two-point correlation function or radial distribution function $S_2(r)$. However, this function $S_2(r)$ tends to be insufficient in the presence microstructural inhomogeneities, such as clustering, due to the lack of directional information. This shortcoming is overcome in this paper with the introduction of joint distance (radial) and orientation based two-point correlation functions $S_2(r, \theta)$ towards the development of ESBCs. The resulting $S_2(r, \theta)$-enriched ESBCs are effective in accounting for statistical inhomogeneities in the exterior domain that define the boundary conditions on the SERVE.

Various simulations of microstructural volume elements or MVEs with fiber clustering are conducted in this paper with different boundary conditions. The studies clearly show that the SERVE with ESBCs are significantly smaller in the converged size compared to the other boundary conditions for homogenized material response. Finally, a comparison is made with the statistical volume element (SVE) method. The SVE method requires larger sample SVE sizes ($\Omega^{sve_l} \approx 200$ μm) and a number of instantiations to converge to the accurate homogenized stiffness. In comparison, a SERVE $\Omega^{serve} \approx 40$ μm subjected to ESBCs requires only one instantiation for predicting the converged stiffness. The proposed method is proved to be a novel way of modeling nonuniform elastic materials for evaluating effective response functions.

Acknowledgments

This work has been supported through a grant No. FA9550-12-1-0445 to the Center of Excellence on Integrated Materials Modeling (CEIMM) at Johns Hopkins University awarded by the AFOSR/RSL Computational Mathematics Program (Manager Dr. A. Sayir) and AFRL/RX (Monitors Drs. C. Woodward and C. Przybyla). These sponsorships are gratefully acknowledged. Computing support by the Homewood High Performance Compute Cluster (HHPC) and Maryland Advanced Research Computing Center (MARCC) is gratefully acknowledged.

Appendix A. Eshelby tensors for circular cylindrical fibers

For a cylindrical fiber of circular cross-section with a radius a and centroid at $\mathbf{x}^I$, the interior and exterior Eshelby tensors S_{ijkl} and $\hat{G}_{ijkl}\left(\mathbf{x}, \mathbf{x}^I\right)$ respectively, are given in Mura (1987) as:

$$S_{ijkl} = \{\alpha\}^T\{\Theta_{ijkl}\}(\theta) \quad \text{and} \quad \hat{G}_{ijkl}\left(\mathbf{x}, \mathbf{x}^I\right) = \{\beta\}^T(r)\{\Theta_{ijkl}\}(\theta) \tag{27}$$

The material-dependent vectors $\{\alpha\}$ and $\{\beta\}$ are:

$$\{\alpha\} = \frac{1}{8\left(1-\nu^M\right)}\begin{Bmatrix} 4\nu^M - 1 \\ 3 - 4\nu^M \\ 0 \\ 0 \\ 0 \end{Bmatrix},$$

$$\{\beta\}(r) = \frac{\rho^2}{8\left(1-\nu^M\right)}\begin{Bmatrix} -2\left(1+2\nu^M\right)+9\rho^2 \\ 2-3\rho^2 \\ 4(1+2\nu^M)-12\rho^2 \\ 4-12\rho^2 \\ 16-24\rho^2 \end{Bmatrix}$$

Here $\rho = \frac{a}{r}$ with $r = |\mathbf{x} - \mathbf{x}^I|$ and $\theta = \angle(\mathbf{x} - \mathbf{x}^I)$, $\mathbf{x}$ being a generic field point. The parameter ν^M is the Poisson's ratio of the matrix material. The circumference basis tensor is given as:

$$\{\Theta_{ijkl}\}(\theta) = \begin{Bmatrix} \delta_{ij}\delta_{kl} \\ \delta_{ik}\delta_{jl} + \delta_{il}\delta_{jk} \\ \delta_{ij}n_k n_l \\ n_i n_j \delta_{kl} \\ n_i n_j n_k n_l \end{Bmatrix}, \quad \text{where} \quad \begin{Bmatrix} n_1 \\ n_2 \\ n_3 \end{Bmatrix} = \begin{Bmatrix} \cos\theta \\ \sin\theta \\ 1 \end{Bmatrix}$$

For the cylindrical fiber of circular cross-section the interior and exterior displacement-transfer tensors are given by:

$$T_{ijk}\left(\mathbf{x}, \mathbf{x}^I\right) = \{\eta\}^T(r)\{\Psi_{ijk}\}(\theta) \quad \text{and} \quad D_{ijk}\left(\mathbf{x}, \mathbf{x}^I\right) = \{\gamma\}^T(r)\{\Psi_{ijk}\}(\theta) \tag{28}$$

where

$$\{\eta\}(r) = a\frac{\rho}{8\left(1-\nu^M\right)}\begin{Bmatrix} 4\nu^M - 1 \\ 3 - 4\nu^M \\ 0 \end{Bmatrix},$$

$$\{\gamma\}(r) = a\frac{\rho}{8\left(1-\nu^M\right)}\begin{Bmatrix} -2\left(1-2\nu^M\right)+\rho^2 \\ 2\left(1-2\nu^M\right)+\rho^2 \\ 4\left(1-\rho^2\right) \end{Bmatrix}$$

and

$$\{\Psi_{ijk}\}(\theta) = \begin{Bmatrix} n_i\delta_{jk} \\ n_j\delta_{ik} + n_k\delta_{ij} \\ n_i n_j n_k \end{Bmatrix}$$

References

Al-Ostaz, A., Diwakar, A., Alzebdeh, K., 2007. Statistical model for characterizing random microstructure of inclusionmatrix composites. J. Mater. Sci. 42 (16), 7016–7030.

Bednarcyk, B.A., Aboudi, J., Arnold, S.M., 2015. Analysis of fiber clustering in composite materials using high-fidelity multiscale micromechanics. Int. J. Solids Struct. 69–70, 311–327.

Böhm, H.J., 2004. A short introduction to continuum micromechanics. In: Böhm, H.J. (Ed.), Mechanics of Microstructured Materials: CISM Courses and Lectures, vol. 464. Springer Wien NY, pp. 1–40.

Chung, P.W., Tamma, K.K., Namburu, R.R., 2000. A finite element thermo-viscoelastic creep for heterogeneous structures with dissipative correctors. Fin. Elem. Anal. Des. 36, 279–313.

Eshelby, J.D., 1957. The determination of the elastic field of an ellipsoidal inclusion and related problems. Proc. R. Soc. London A241, 376–396.

Everett, R., 1993. Analysis and modeling of fiber clustering in composites using n–tuples. Scr. Metall. Mater. 28 (6), 663–668.

Feyel, F., Chaboche, J.H., 2000. FE^2 multiscale approach for modelling the elastoviscoplastic behaviour of long fibre SiC/Ti composite materials. Comput. Methods Appl. Mech. Eng. 183, 309–330.

Fish, J., Shek, K., 2000. Multiscale analysis of composite materials and structures. Comp. Sci. Technol. 60, 2547–2556.

Fullwood, D., Niezgoda, S., Kalidindi, S., 2008. Microstructure reconstructions from 2-point statistics using phase-recovery algorithms. Acta Mater. 56, 942–948.

Ghosh, S., 2011. Micromechanical Analysis and Multi-Scale Modeling Using the Voronoi Cell Finite Element Method. CRC Press/Taylor & Francis.

Ghosh, S., Kubair, D., 2016. Exterior statistics based boundary conditions for representative volume elements of elastic composites. J. Mech. Phys. Solids 96, 1–24.

Ghosh, S., Lee, K., Moorthy, S., 1995. Multiple scale analysis of heterogeneous elastic structures using homogenization theory and Voronoi cell finite element method. Int. J. Solids Struct. 32 (1), 27–62.

Ghosh, S., Lee, K., Moorthy, S., 1996. Two scale analysis of heterogeneous elastic–plastic materials with asymptotic homogenization and Voronoi cell finite element model. Comput. Methods App. Mech. Eng. 132 (1–2), 63–116.

Gommes, C., Jiao, Y., Torquato, S., 2012. Density of states for a specified correlation function and the energy landscape. Phys. Rev. Lett. 108, 080601–1–5.

Guedes, J.M., Kikuchi, N., 1991. Preprocessing and postprocessing for materials based on the homogenization method with adaptive finite element methods. Comput. Methods App. Mech. Eng. 83, 143–198.

Guo, E.-Y., Chawla, N., Jing, T., Torquato, S., Jiao, Y., 2014. Accurate modeling and reconstruction of three-dimensional percolating filamentary microstructures from two-dimensional micrographs via dilation-erosion method. Mater. Charact. 89, 33–42.

Hazanov, S., Huet, C., 1994. Order relationships for boundary conditions effect in heteogeneous bodies smaller than the representative volume. J. Mech. Phys. Solids 42, 1995–2011.

Heinrich, C., Aldridge, M., Wineman, A.S., Kieffer, J., Waas, A.M., Shahwan, K., 2012. The influence of the representative volume element (rve) size on the homogenized response of cured fiber composites. Modell. Simul. Mat. Sci. Eng. 20 (7).

Hill, R., 1963. Elastic properties of reinforced solids: some theoretical principles. J. Mech. Phys. Solids 11, 357–372.

Hill, R., 1967. The essential structure of constitutive laws for metal composites and polycrystals. J. Mech. Phys. Solids 15, 79–95.

Jiao, Y., Stillinger, F., Torquato, S., 2007a. Modeling heterogeneous materials via two–point correlation functions: basic principles. Phys. Rev. E 76, 031110.

Jiao, Y., Stillinger, F., Torquato, S., 2007b. A superior descriptor of random textures and its predictive capacity. Proc. Nat. Acad. Sci. USA 106 (42), 17634–17639.

Kanit, T., Forest, S., Galliet, I., Mounoury, V., Jeulin, D., 2003. Determination of the size of the representative volume element for random composites: statistical and numerical approach. Int. J. Solids Struct. 40 (13–14), 3647–3679.

Kouznetsova, V., Geers, M.G.D., Brekelmans, W.A.M., 2002. Multi-scale constitutive modelling of heterogeneous materials with a gradient-enhanced computational homogenization scheme. Int. J. Numer. Methods Eng. 54, 1235–1260.

Lenthe, W., Pollock, C., 2014. Microstructural characterization of unidirectional composites. Private Communications.

Liu, K.C., Ghoshal, A., 2014. Validity of random microstructures simulation in fiber-reinforced composite materials. Composites Part B 57, 56–70.

Liu, X., Shapiro, V., 2015. Random heterogeneous materials via texture synthesis. Comput. Mater. Sci 99, 177–189.

McDowell, D.L., Ghosh, S., Kalidindi, S.R., 2011. Representation and computational structure-property relations of random media. JOM, TMS 63 (3), 45–51.

Mura, T., 1987. Micromechanics of Defects in Solids, second ed. Kluwer Academic Publishers and Martinus Nijhoff.

Niezgoda, S., Fullwood, D., Kalidindi, S., 2008. Delineation of the space of 2-point correlations in a composite material system. Acta Mater. 56 (18), 5285–5292.

Niezgoda, S., Turner, D., Fullwood, D., Kalidindi, S., 2010. Optimized structure based representative volume element sets reflecting the ensemble-averaged 2-point statistics. Acta Mater. 58, 4432–4445.

Ostoja-Starzewski, M., 2007. Microstructural randomness and scaling in mechanics of materials. Chapman and Hall/CRC.

Patterson, A., 1939. Homometric structures. Nature 143, 939–940.

Patterson, A., 1943. Ambiguities in the x-ray analaysis of crystal structures. Phys. Rev. 68 (5–6), 195–201.

Pyrz, R., 1994. Correlation of microstructure variability and local stress-field in 2-phase materials. Mat. Sci. Eng. A 177 (1–2), 253–259.

Romanov, V., Lomov, S., Swolfs, Y., Orlova, S., Gorbatikh, L., Verpoest, I., 2013. Statistical analysis of real and simulated fibre arrangements in unidirectional composites. Composites Sci. Technol. 87, 126–134.

Rozman, M., Utz, M., 2002. Homometric structures. Phys. Rev. Lett. 89 (13), 135501–1–4.

Shan, Z.H., Gokhale, A.M., 2002. Representative volume element for non-uniform micro-structure. Comput. Mater. Sci. 24 (3), 361–379.

Stroeven, M., Askes, H., Sluys, L.J., 2004. Numerical determination of representative volumes for granular materials. Comput. Meth. Appl. Mech. Eng. 193 (30–32), 3221–3238.

Swaminathan, S., Ghosh, S., Pagano, N., 2006. Statistically equivalent representative volume elements for unidirectional composite microstructures: Part i-without damage. J. Composite Mater. 40 (7), 583–604.

Swaminathan, S., Pagano, N., Ghosh, S., 2006. Statistically equivalent representative volume elements for unidirectional composite microstructures: Part ii-with interfacial debonding. J. Composite Mater. 40 (7), 605–621.

Terada, K., Kikuchi, N., 2000. Simulation of the multi-scale convergence in computational homogenization approaches. Int. J. Solids Struct. 37, 2285–2311.

Tewari, A., Gokhale, A., Spowart, J., Miracle, D., 2004. Quantitative characterization of spatial clustering in three-dimensional microstructures using two-point correlation functions. Acta Mater. 52 (2), 307–319.

Thomas, M., Boyard, N., Perez, L., Jarny, Y., Delaunay, D., 2008. Representative volume element of anisotropic unidirectional carbon-epoxy composite with high–fibre volume fraction. Composites Sci. Technol. 68 (15–16), 3184–3192.

Torquato, S., 1997. Effective stiffness tensor of composite media-i. exact series expansions. J. Mech. Phys. Solids 45 (9), 1421–1448.

Torquato, S., 2002. Random Heterogeneous Materials; Microstructure and Macroscopic Properties. Springer-Verlag, New York.

Wilding, S.E., Fullwood, D.T., 2011. Clustering metrics for two-phase composites. Comput. Mater. Sci. 50 (7), 2262–2272.

Willoughby, N., Parnell, W., Hazel, A., Abrahams, I., 2012. Homogenization methods to approximate the effective response of random fibre-reinforced composites. Int. J. Solids Struct. 49 (13), 1421–1433.

Yeong, C., Torquato, S., 1998. Reconstructing random media. Phys. Rev. E 57 (1), 495–506.

Yin, X., To, A., McVeigh, C., Liu, W., 2008. Statistical volume element method for predicting microstructureconstitutive property relations. Comput. Methods Appl. Mech. Eng. 197, 3516–3529.

Zangenberg, J., Larsen, J.B., Astergaard, R.C., Brandsted, P., 2012. Methodology for characterisation of glass fibre composite architecture. Plast. Rubber Composites 41 (4/5), 187–193.

Zeman, J., Sejnoha, M., 2007. From random microstructures to representative volume elements. Modell. Simul. Mater. Sci. Eng. 15 (4), S325–S335.

Zohdi, T.I., Wriggers, P., 2004. An Introduction to Computational Micromechanics. Springer.